UNIVERSITÀ DEGLI STUDI DI MILANO

FACOLTÀ DI SCIENZE E TECNOLOGIE

CORSO DI LAUREA MAGISTRALE IN FISICA

Transient grating spectroscopy with a magnetic probe: a study on phonon-driven magnons in a ferromagnetic thin film

Relatore:
Prof. Giorgio Rossi

Correlatori:
Dr. Giancarlo Panaccione
Dr. Riccardo Cucini

Tesi di laurea di:
Marta Brioschi

Matricola:
939954

Codice PACS: 78.47.jd

ANNO ACCADEMICO 2019-2020

Riassunto

I materiali e le eterostrutture con proprietà magnetoelastiche sono interessanti sia per studi di fisica fondamentale che per applicazioni tecnologiche. In particolare, presentano grande potenzialità per applicazioni in dispositivi spintronici a basso consumo energetico, poiché le onde acustiche possono generare onde di spin coerenti e a basso smorzamento attraverso il fenomeno della magnetostrizione inversa, che consiste in variazioni della magnetizzazione conseguenti alle deformazioni di reticolo. Poiché i metodi ottici sono versatili e non distruttivi, abbiamo implementato e applicato un approccio completamente ottico per studiare l'accoppiamento magnetoelastico in un film ferromagnetico cresciuto su un substrato di vetro.

Il presente lavoro di tesi è stato svolto presso il laboratorio NFFA-SPRINT dello IOM-CNR ospitato nella sala sperimentale del laser a elettroni liberi FERMI@Elettra a Trieste, dove ho attivamente contribuito alla costruzione e caratterizzazione di un nuovo setup sperimentale in grado di combinare la spettroscopia transient grating (TG) con la polarimetria Faraday risolta in tempo.

La spettroscopia TG è una tecnica ottica non lineare pompa-sonda (appartenente alla classe della spettroscopia four-wave mixing) in cui due impulsi laser corti e sovrapposti sia temporalmente che spazialmente interferiscono sul campione, generando il cosiddetto TG. Nel caso specifico, gli impulsi di pompa sono generati dalla sorgente laser PHAROS presente nel laboratiorio NFFA-SPRINT, che genera impulsi di 300 fs a una lunghezza d'onda di 1030 nm. Per deformazioni reticolari impulsive di natura termoelastica ed elettrostrittiva, il TG eccita fononi coerenti aventi un vettore d'onda determinato dalla periodicita del TG, che inducono una modulazione spaziale e periodica delle costanti ottiche del materiale. Questa tecnica rappresenta dunque un modo efficiente per generare onde acustiche superficiali di frequenza regolabile. Il fascio di probe (di lunghezza d'onda 515 nm), ottenuto mediante generazione di seconda armonica dell'output del PHAROS, è diffratto dalla modulazione indotta dal TG, in riflessione e in transmissione. Misurando l'intensità del fascio diffratto a diversi ritardi temporali rispetto alla pompa ottica, è possibile estrarre informazioni circa la dinamica indotta nel campione dal TG.

Le onde acustiche stazionarie generate nel substrato si accoppiano con la magnetizzazione del film sottile, generando un'onda coerente di spin avente la stessa lunghezza d'onda delle onde acustiche. L'effetto Faraday risolto in tempo sonda la componente fuori piano della magnetizzazione, rilevando la variazione di polarizzazione del fascio trasmesso e fornendo informazioni circa la dinamica di magnetizzazione indotta dal TG. La possibilità di osservare tali variazoni in polarizzazione è direttamente legata alla parziale demagnetizzazione del campione indotta dal profilo di temperatura, anch'esso dovuto al TG. Aggiungendo al meccanismo di eccitazione del TG e alla polarimetria Faraday un campo magnetico esterno nel piano del film, è possibile estrarre la magnetizazzione di saturazione del film sottile. Infatti, i momenti magnetici del film sottile in un campo esterno precedono a una frequenza data dalla formula di Kittel, che descrive la risonanaza ferromagnetica (FMR) in questo caso specifico e dipende sia dall' intensità del campo esterno che dalla magnetizzazione di saturazione. Variando il campo magnetico esterno in modo che la

frequenza di Kittel risulti uguale a quella delle onde acustiche generate dal TG, si raggiunge la FMR per interazione fononica, la quale comporta un aumento in intensità dell'effetto Faraday. La magnetizzazione di saturazione è ottenuta confrontando e affinando l'inviluppo di tali risonanze con la formula di Kittel.

L'apparato sperimentale è stato testato su un campione di nickel in forma di film sottile di 40 nm cresciuto su un substrato di quarzo fuso. La caratterizzazione acustica del substrato, eseguita usando la tecnica della spettroscopia TG, mostra che il TG genera nel campione due onde acustiche di superfice, nello specifico l'onda di Rayleigh e la cosiddetta surface skimming longitudinal wave, le cui frequenze sono variabili a seconda della periodicità del TG. Come atteso, le risonanze dovute alla FMR per interazione fononica sono state osservate ed è stata ottenuta una magnetizzazione di saturazione di 238 ± 20 kA m^{-1}. Abbiamo infine osservato fenomeni di ordine superiore dovuti alla modulazione parametrica della dinamica di magnetizzazione, quali down-conversion, up-conversion e frequency mixing, ottenedo conferma dell'alta qualità delle prestazioni del setup sperimentale, che può essere dunque considerato pronto per essere impiegato nello studio di sistemi più complessi.

Abstract

Materials and heterostructures that exhibit coupling between elastic and magnetic degrees of freedom are of both fundamental and technological interest. In particular, they have great potential for novel energy-efficient spintronic devices because acoustic waves can generate coherent and long-living spin waves through inverse magnetostriction, which consists in variations in the magnetization due to lattice deformations. As optical methods are versatile, non-invasive and contactless, an all-optical approach has been implemented and applied to study magnetoelastic coupling in a ferromagnetic film on a glass substrate.

The present thesis work was performed at the NFFA-SPRINT facility of IOM-CNR in the Fermi@Elettra hall at Trieste, where I actively contributed to the realization and characterization of an all new experimental setup which is able to combine transient grating spectroscopy with a time-resolved Faraday polarimetry.

Transient grating spectroscopy is a nonlinear optical pump-probe technique belonging to the class of four-wave mixing, in which two short, spatially and temporally overlapped laser pump pulses interfere on the sample, generating the so-called transient grating (TG). In the specific case, the pump pulses are generated by the PHAROS laser source of NNFA-SPRINT, that generates 300 fs-long pulses of wavelength $\lambda = 1030$ nm. By impulsive thermoelastic and electrostrictive lattice deformations, it excites coherent phonons with a wave vector strictly related to the TG periodicity, that in turn periodically modulate the optical constants of the sample. Therefore, this technique allows to efficiently excite frequency-tunable standing (surface) acoustic waves. The probe beam (wavelength $\lambda = 515$ nm), which is obtained by second harmonic generation of the PHAROS output, is diffracted by this TG-induced modulation in transmission and in reflection geometry. By measuring the intensity of the diffracted beam at selected time delays respect to the pump, one gets a time-resolved information about the TG-induced dynamics.

The standing acoustic waves generated in the substrate couple with the magnetic degrees of freedom of the thin film, generating a coherent spin wave of equal wavelength. The time-resolved Faraday effect probes the out-of-plane component of the magnetization by detecting the transmitted light polarization changes, providing information about the TG-induced magnetization dynamics. The measured changes of the magnetization are closely related to the temperature-induced partial demagnetization of the sample due to the TG-induced temperature profile. By performing TG excitation and Faraday polarimetry with an in-plane external applied magnetic field, it is possible to derive the saturation magnetization of the film. The magnetic moments of a ferromagnetic thin film in an external field precess with a frequency given by the Kittel formula, which describes the ferromagnetic resonance (FMR) in this specific case and depends on both external field and saturation magnetization. By tuning the applied magnetic field intensity so that the frequency of the acoustic waves matches the Kittel frequency, elastically driven FMR is achieved and great enhancement of the Faraday effect magnitude is expected. The saturation magnetization was obtained by fitting the envelope of these resonances with the Kittel formula.

The setup has been tested on a 40 nm Ni thin film grown on a fused quartz substrate. The acoustical characterization of the sample by TG spectroscopy shows that the TG generates two surface acoustic waves, namely the Rayleigh Surface Acoustic Wave and the Surface Skimming Longitudinal Wave, whose frequencies are tunable by varying the TG periodicity. As expected, resonances due to acoustically-driven FMR have been observed and the obtained saturation magnetization is 238 ± 20 $\mathrm{kA\,m^{-1}}$. Finally, higher order effects due to parametric modulation of the magnetization dynamics, such as down-conversion,up-conversion and frequency mixing, were observed, giving evidence of the high quality of the newly built setup and it readiness for performing research on complex quantum material systems.

Indice

Introduction and motivation

The information messenger of current electronic devices is the electron charge, through its transport and accumulation processes in matter. When the size of the active devices is reduced to some nm, the quantum behaviour emerges and dissipation issues lead to breakdown of ideal transistor operation [1]. Spintronics, which is still nowadays an active field of research, has been proposed as an alternative approach where both spin and charge of conduction electrons vehiculate the information. The main advantage in exploiting spin currents is that no charge motion is involved, and no heat is dissipated by Joule effect. However, spintronics is challenging on several aspects. In spin-wave-based logic data processing is achieved by controlling amplitude and phase of the spin wave. Therefore, spin wave decoherence and its intrinsic magnetic damping upon propagation in the material represent a great obstacle [2]. Therefore, being able to control magnetism is the basis to achieve compact and energy-efficient spintronic devices. In particular, strain-controlled magnetism seems to be a particularly efficient option [3] that deserves a thorough investigation.

Surface acoustic waves have been extensively used to investigate the fundamentals of phonon-magnon coupling in ferromagnetic thin films [3, 4, 5, 6]. Indeed, acoustic waves can induce coherent and long-living spin waves through inverse magnetostriction, which consists in variation of the magnetization due to lattice deformations. Acoustic waves can be generated in many different ways, and several approaches can be adopted. Most of the studies involve a pair of interdigitated transducers (IDTs) on a piezoelectric substrate [4, 5]. An interdigitated transducer consists in two interlocking comb-shaped metallic electrodes. The so-called input transducer converts a periodic electric signal into lattice deformation with equal periodicity of the substrate via piezoelectric effect, generating surface acoustic waves (SAWs) propagating in a well defined direction. Upon propagation of the SAWs, the mechanical stress is converted into an electric signal by the so-called output IDT, which gives information about the excited SAWs. In magnetoelastic studies, the ferromagnetic thin film is usually deposited between the two IDTs, in the middle of the piezoelectric substrate. The coupling between the thin film magnetic degrees of freedom and the generated SAWs is measured by changes in the complex transmission coefficient [4], which give an indication of the absorbed elastic energy inducing a magnetization dynamics. These devices have been proved to be effective in achieving all-elastically driven ferromagnetic resonance (FMR), where radio-frequency (RF) SAW-induced elastic deformation replaces the traditionally applied RF electromagnetic field. However, this kind of devices have some limitations. Since they are

directly placed on the piezoelectric substrate and the thin film is grown directly on it, they are quite invasive and limited to the system under analysis. Furthermore, they can only generate SAWs with frequencies compatible with the IDT designed periodic pattern, which itself has practical limitations. The frequency range of operation of SAW transducers is between 50 MHz and several GHz [7].

In this thesis an all-optical approach is adopted. As optical methods are not constrained by such complicated structures on the substrate, they result more versatile and less invasive with respect to the transducer-based approach. Specifically, we exploited the transient grating (TG) spectroscopy [8], a nonlinear optical pump-probe technique belonging to the class of four-wave mixing spectroscopy. Two short, spatially and temporally overlapped pump pulses interfere on the sample surface, generating the so-called TG. It periodically modulates the optical properties and excites coherent phonons through impulsive thermoelastic and electrostrictive lattice deformations, whose wave vector is strictly related to the TG periodicity. The probe consists in a third pulsed beam, typically of different wavelength, which is diffracted by the superficial TG-induced modulation. The variation of the probe intensity at different time delays provides time-resolved information about the TG-induced dynamics.

The TG technique represents an efficient way to generate coherent spin waves in ferromagnetic thin films. In general, it is quite difficult to obtain coherent optical manipulation of the spin dynamics in metals, since it requires discrete energy levels such as in magnetic semiconductors and insulators. Electron states in solids have a finite lifetime due to nonradiative transitions caused by electron-electron scattering, which are very short in transition metals (~ 5 fs) [9]. Relaxation of the excited state in electron-electron scattering leads to loss of spin coherence. Therefore, the generation of coherent spin dynamics in metals requires ultrashort laser pulses [9]. However, in a ferromagnetic thin film grown on a glass substrate, it can be achieved also with longer pulses by exploiting the magnetoelastic coupling between the thin film magnetization and the acoustic waves excited with the TG technique in the substrate. Therefore, the spin wave will live as long as the SAWs persist in the sample. Furthermore, it is possible to probe simultaneuosly the TG-induced acoustic and magnetic dynamics with sub-picosecond resolution. To monitor the magnetization dynamics, we use a time resolved Faraday polarimetry, which is relatively easy to implement in our experimental setup design. Specifically, in our geometrical configuration, the out-of-plane component of the magnetization is probed as a function of time, giving information about the dynamics induced by the coupling between the acoustic and the magnetic degrees of freedom.

Combining these two experimental techniques with an in-plane external magnetic field, it is also possible to extract some information about the magnetic properties of the sample, such as the saturation magnetization. This is possible considering that the magnetic moments of a ferromagnetic thin film in an external field precess with a frequency given by the Kittel formula [10], which describes the FMR in this specific case. When the applied field is such that the frequency of the TG-generated acoustic waves matches the Kittel frequency, elastically driven FMR is achieved and great enhancement of the Faraday effect magnitude is expected [6]. The envelope

of such resonances as a function of the applied field gives the Kittel curve, that parametrically depends on the saturation magnetization.

Finally, laser-induced TG modulation can generate strain amplitudes larger by almost an order of magnitude than transducer-based methods [3], enabling spin wave studies in the nonlinear regimes [11].

The aim of the experimental work presented in this thesis is proving that the experimental setup we built, which is based on a contactless approach, is able to combine TG spectroscopy with a magnetic probe in order to perform magnetoelastic studies on a simple system.

The present work is divided as follows:

- Chapter 1 gives an overview of the TG and Faraday polarimetry experimental techniques. It also introduces the TG-generated SAW and how they couple with the magnetic degrees of freedom.

- Chapter 2 provides a description of the laser sources and the experimental setup we built, along with its characterization and details regarding the design, calibration and fabrication of some components.

- Chapter 3 describes the sample preparation and presents the first experimental results.

Capitolo 1

Theoretical background

1.1 Surface acoustic waves

SAWs are acoustic waves propagating along the surface of a material exhibiting elasticity, with an amplitude that typically decays exponentially with depth into the material. SAW can be classified accordingly to the nature of the surface strain, which can be longitudinal, transverse or both of them. This section describes the two SAWs of interest in this study, namely the Rayleigh Surface Acoustic Wave (RSAW) and the Surface Skimming Longitudinal Wave (SSLW) and provides a brief introduction to SAWs in thin films.

The Rayleigh Surface Acoustic Wave

The RSAW was predicted in 1885 by Lord Rayleigh, who worked on wave solutions in a semi-infinite continuum. Indeed, as the wavelength of the RSAW is much longer than the atomic bonds, the material can be treated classically as a continuum occupying an half space. This kind of SAW is strongly confined to the surface and the penetration depth is of the order of its wavelength; as a consequence, the damping is reduced with respect to bulk waves. In isotropic solids these waves cause the surface atoms to move in ellipses in planes normal to the surface and parallel to the direction of propagation, which means that RSAWs include both longitudinal and transverse displacements [13]. Figure 1.1 depicts such motion.

RSAWs have a lower speed with respect to both longitudinal and transverse waves, by a factor dependent on the elastic constants of the material; a complete calculation of the acoustic wave dispersion can be found in Reference [14]. The typical speed of RSAWs spans from $2-5$ km s^{-1} in metals until reaching its highest value of 10 km s^{-1} in diamond [14]. Among their many application, RSAWs are used in non-destructive testing, for example to investigate mechanical and structural properties of materials [15], and they are exploited in digital devices, such as filters [13], sensors of pressure, temperature, humidity, etc. [16] and magnetic sensors [17].

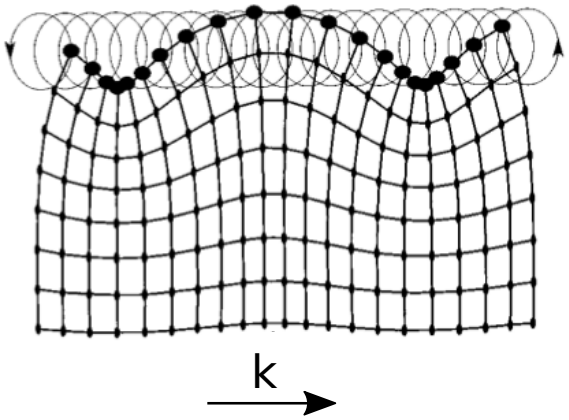

Figura 1.1: Schematic illustration of the particle's motion in a RSAW wave propagating on the free surface of an infinite half-space. Particles move in ellipses in planes normal to the surface and parallel to the direction of propagation $\vec{k}$. Adapted from [12]

Surface Skimming Longitudinal Wave

The other type of SAW of interest in this thesis work is the SSLW. Unlike what happens for RSAW, both the formal description and experimental studies on SSLWs are still subject to controversy [18]. A SSLW is a SAW that penetrates into the bulk with a very small angle with respect to the surface [19]. It can be seen as a wave that propagate along the surface coupled to a bulk shear wave. Being in fact a bulky wave, it propagates faster with respect to SAWs. Intuitively, the penetration length of the SSLW is greater than the one of the RSAW, but it seems that there is no precise relationship with its frequency. Even if there is still a lot to learn about this type of acoustic waves, many SSLW applications are reported in literature and most of them involve ITD on a piezoelectric substrate [20, 21, 22]. This is not surprising because when SSLWs were observed for the very first time, they were considered unwanted bulk waves in ITD devices [23].

Acoustic waves in thin films

Let's now analyze acoustic waves in thin films [24]. Thin films are planar acoustic waveguides and they can sustain multiple dispersive modes, whose features depend on the specific composition and on any residual stresses. The normal modes can be computed from the equation of motion and boundary conditions. Neglecting nonlinear effects, displacements in each part of the waveguide must satisfy

$$\frac{\partial^2 u_j}{\partial t^2} = \frac{c_{ijkl}}{\rho}\frac{\partial^2 u_k}{\partial x_i \partial x_l} + \frac{\partial}{\partial x_i}\left(\sigma_{ik}^{(r)}\frac{\partial u_j}{\partial x_k}\right) \tag{1.1}$$

where u is the displacement, c is the stiffness tensor, ρ the density of the thin film and $\sigma^{(r)}$ the residual stress tensor. Of course, boundary condition are different depending on whether the thin film is free standing or bound to a substrate. In the first case the normal components of the stress tensor vanish, while they are continuous at the interface film-substrate when are intimately bound one to another. Therefore, by

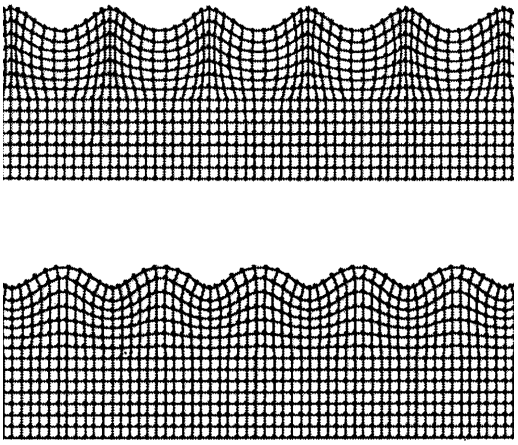

Figura 1.2: Distortions given by the lowest guided mode in a thin film strongly bounded to the substrate for $hq = 1.5$ (top panel) and $hq = 0.8$ (bottom panel). The more $hq \to 0$, the closer the lowest guided mode velocity to the velocity of the RSAW in the substrate and, therefore, the smallest the perturbation given by the thin film presence. As $hq \sim 0.01$ and the effect of the thin film on the SAWs of the substrate is negligible. Figure adapted from [24].

solving Equation 1.1 with the proper boundary conditions, it is possible to determine the phase velocity v_{ph} of the waveguide modes depending on the acoustic wave vector $\vec{q}$.

In particular, for waveguides that include a single thin film of thickness h, it can be shown that the phase velocities only depend on the product hq, namely $v_{ph} \propto hq$. In our case, we have films directly grown on the substrate and $hq \sim 0.01$, since $h \sim 10$ nm and $q \sim \mu\text{m}^{-1}$. For a tightly bound thin film the modes are strictly guided only for velocities less than the transverse velocity in the substrate and for $hq \to 0$ the v_{ph} of the lower mode tends to the velocity of the RSAW of the substrate. Figure 1.2 shows the lowest mode surface distortion of a thin film strongly bound to the substrate for $hq = 1.5$ and $hq = 0.8$. The bigger the wavelength of the RSAW, the smaller will be the effect of the film on the substrate. Detailed calculations can be found in Reference [24].

1.2 Transient Grating Spectroscopy

TG spectroscopy can be classified within the more general framework of the four-wave mixing spectroscopy [25]. Its many applications are an indication of its great versatility: it has been used to acoustically characterize thin film [24], to study acoustic and thermal properties of polymers [26], to investigate the dynamics of complex liquids [8], to learn about gas phase velocity distributions and collisional effects [27, 28] and, more recently, it has been applied in magnetoelasticity studies [6, 29, 30].

A schematic picture of a TG experiment is illustrated in Figure 1.3. In a TG experiment a single pulsed laser beam is split to obtain two laser pulses, which interfere

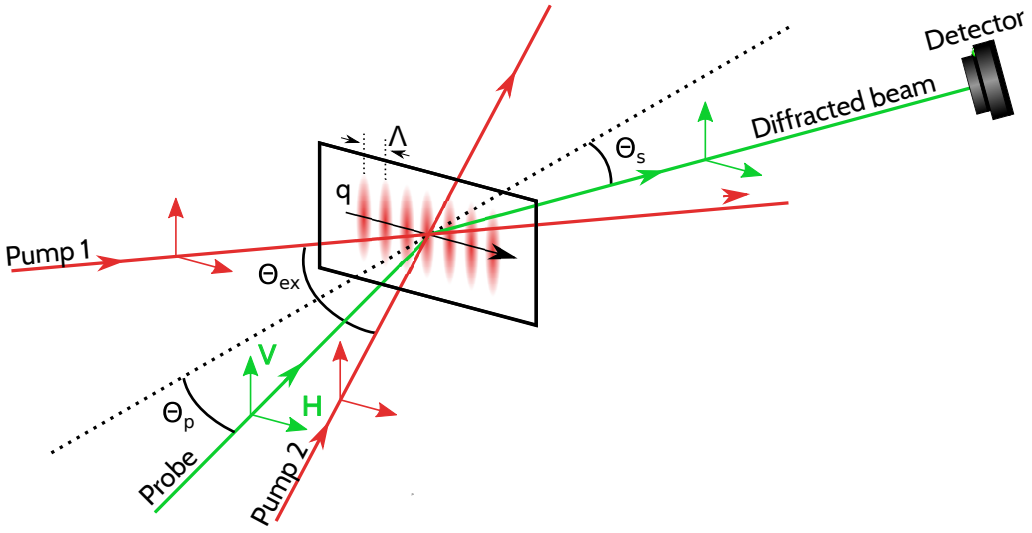

Figura 1.3: TG experiment in transmission geometry.

within the sample to generate the so-called TG, a spatially periodic variation of the optical material properties by standing-wave excitation of some material phononic modes [31, 32]. The spatial modulation of the material optical properties acts as a diffraction grating lasting the time of overlapping pulses. Its spatial extension is given by the pulses temporal length and its efficiency depends on the overlap area of the two pump pulses. This modulation is probed by a third laser beam of different wavelength, which can be a pulsed or a continuous-wave field. It impinges on the TG-induced modulation and it is diffracted by it. A measurement of the intensity of the diffracted beam at selected time delays with respect to the pump allows the acquisition of dynamic information on the relaxing TG, and consequently of the properties of the excited modes.

An important parameter of the spatial modulation is the wave vector $\vec{q}$, given by the difference of the two pump wavevectors $\vec{k}_2 - \vec{k}_1 = \vec{q}$. Its modulus depends on the TG periodicity (or pitch) Λ, the wavelength of the pump pulses λ_{ex} and their incidence angle θ_{ex} on the sample:

$$q = \frac{2\pi}{\Lambda} = \frac{4\pi \sin(\theta_{ex}/2)}{\lambda_{ex}} \tag{1.2}$$

Depending on the grating spacing-depth ratio, the gratings can be classified into thin and thick gratings. In the case of a thin grating, which has the depth smaller or the same order of its pitch Λ, the probe can be diffracted for any incidence angle and the usual diffraction law is valid

$$\Lambda(\sin\theta_p - \sin\theta_s) = m\lambda_p \qquad\qquad m = \pm 1, \pm 2... \tag{1.3}$$

where λ_p is the probe wavelength and θ_p and θ_s are respectively the probe incidence angle and the diffraction (scattering) angle.

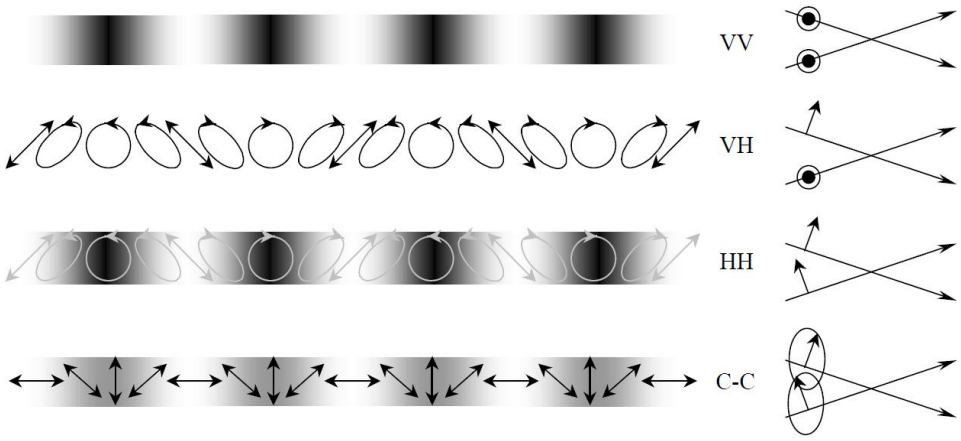

Figura 1.4: Different types of gratings depending on the pump polarization. Image from [33].

On the other hand, a thick grating has a depth much larger than its pitch Λ. This kind of grating can be probed efficiently only if the wave vector of the probe $\vec{k}_p$ and the scattered beam $\vec{k}_s$ obey the Bragg condition

$$\vec{k}_s - \vec{k}_p = m\vec{q} \qquad\qquad m = \pm 1, \pm 2... \tag{1.4}$$

If the frequencies of excited modes are very low with respect to the optical frequency, it holds $|\vec{k}_p| \simeq |\vec{k}_s|$. Thus the wavelength of the probe λ_p and equation 1.2 fix completely the directions of the probe and scattered beam

$$\vec{k}_s - \vec{k}_p = \pm\vec{q} \tag{1.5}$$

Types of gratings and dynamical processes

Depending on the pump polarization, different types of gratings can be generated [33]. Defining the scattering plane as the plane containing the pump and the probe beams, the polarization will be considered vertical (V) if it is orthogonal to it, horizontal (H) if parallel. The main possible polarization configurations are VV, VH, HH and circular-circular (CC). When the two pumps have at least a vertical polarization component, the interference generates an intensity TG along the $\vec{q}$ direction. A pure intensity grating is therefore achieved in the VV configuration. When working in the VH arrangement, only a polarization grating is induced: along the $\vec{q}$ direction the interference field gradually changes its polarization from linear, to circular, to linear an so on. In the HH configuration both polarization and intensity grating are induced simultaneously, while in the CC there still is both the intensity and polarization gratings but the polarization is always linear, it just rotates with the grating periodicity along the $\vec{q}$ direction. Polarization gratings find many applications in spin-related dynamics studies [34, 26]. In this thesis we only focus on pure intensity gratings (VV). The different types of gratings are schematically depicted in Figure 1.4.

Under the hypothesis that the sample has no electronic resonance with the pump, the grating is dominated by the birenfringence-phase contribution, which is related

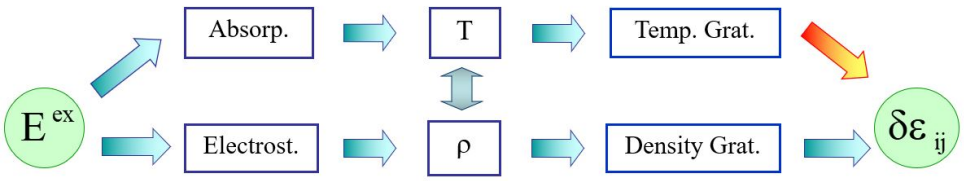

Figura 1.5: The excitation forces and the induced modes in a TG experiment. Image Adapted from [35]

to the modulation of the real part of the refraction index. In this case, which is indeed our case, the optical properties of the sample are modulated by two main interactions [8, 35], schematically summarized in Figure 1.5.

The first one is absorption, which generates a temperature grating. Thanks to the thermal expansion, a density and pressure grating builds up; the result is the generation of two counter-propagating acoustic waves whose superposition is a stationary acoustic wave. The acoustic wave characteristics depends on both $\vec{q}$ and the sample under analysis. The thermal grating relaxes by thermal diffusion following an exponential decay with a characteristic time $\sim$ µs, much longer than both the decay and speed of the acoustic wave.

The second effect is electrostriction, which gives rise to a density grating without any absorption. The effect is based on the dipole moment induced by the interference field. The induced dipoles move towards the areas corresponding to an interference maximum, leading to the formation of compressional zones. This is exactly the opposite of what happens in thermal gratings, where the compression zones spatially corresponds to the interference minima. This means that the acoustic wave launched by the two effects has a $\pi/2$ phase difference.

In our case specific case, absorption prevails on electrostriction.

Transient grating as a four wave mixing process

In the field of non-linear optics there are many exotic effects, and one of the most important is undoubtedly frequency mixing [36, 37]. In these processes a beam of monochromatic light in interaction with atoms can be partially converted into light, whose frequencies are harmonics of the fundamental frequency. Similarly, beams of two or more different frequencies can combine to produce light beams at one or more number of different frequencies. In a more rigorous picture this effect can be explained taking into account the different components of the nonlinear polarization, which generate electromagnetic waves having frequencies different from those of the incident waves [37, 38]. Of course, in such processes, energy and momentum must be conserved. This brings some conditions to the energies and wave vectors of the possible emitted photons, which are dictated by the so-called phase matching condition [39, 40].

Four-wave mixing [41, 8] is a particular case of nonlinear frequency mixing, which arise from the interaction of four coherent optical fields through the third order nonlinear susceptibility tensor $\boldsymbol{\chi}^{(3)}$. In the specific case of a TG experiment the

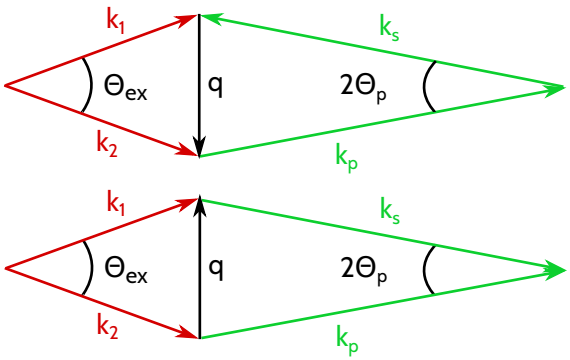

Figura 1.6: Phase matching condition in a TG experiment. As $\vec{k}_s - \vec{k}_p = \pm\vec{q}$, the probe is diffracted in both reflection (top panel) and transmission (bottom panel) geometries.

three incoming beams interact with the medium, giving a nonlinear polarization that becomes the source of the diffracted field.

The scattered (or diffracted) beam is at a very precise angle, due to the phase matching condition. Equation 1.5 together with Figure 1.6 schematically explains why both reflection and transmission geometries are possible.

As the sample has no electronic resonances with any of the electrical fields involved, the pumping and probing processes can be treated separately. It can be proved [8] that the dielectric constant modulation variation induced by the pumps in the sample is

$$\delta\varepsilon(\vec{q},t) \propto \chi^{(3)}(\vec{q},t)\Big[E_{ex,tot}(\vec{q},t)\Big]^2 \tag{1.6}$$

where $E_{ex,tot}(\vec{q},t)$ is the sum of the fields of the two excitation pulses. The measured signal can be expressed as

$$I(\vec{q},t) \propto |E_{ex}^2 E_p \chi^{(3)}(\vec{q},t)|^2 \tag{1.7}$$

where E_{ex} and E_p are respectively the magnitude of the pump and probe fields. Since $\chi^{(3)}$ contains information about how the pump fields interact with sample, the measured TG signal gives a direct insight into the excited modes and their evolution in time.

An experimental example

Let's now analyse a typical experimental TG signal (VV configuration), shown in Figure 1.7. At time delays $\tilde{t} < 0$ the TG signal is zero. At $\tilde{t} = 0$ there is the so-called coherent peak. It is due to the electronic response of the sample given by the temporal (and spatial) overlap of the three pulses. Therefore, it represents the cross-correlation of the pump and probe pulses [28]. The following diffracted probe modulation for $\tilde{t} > 0$ provides a time-resolved information regarding the dynamics induced in the sample. Any dynamics with time scales faster than the pulse duration can not be resolved. The frequency of the excited phonon modes can be easily extracted from the Fourier analysis of the signal, and the error on frequency can be estimated by the FWHM of the Fourier transform peak. The longer the delay line, the smallest the error.

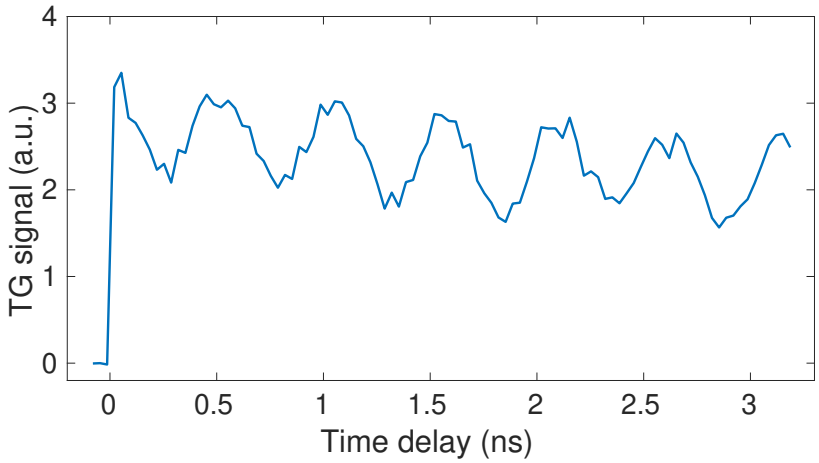

Figura 1.7: Typical trend of a TG signal.

As mentioned earlier, the relaxation time of the thermal grating through thermal diffusion has time scales $\sim$ µs, much larger than the velocity and damping of the acoustic wave. The background of the signal in Figure 1.7 is indeed the system thermal decay seen on a too short timescale. Bigger time delays are needed to get useful information. Experimentally, this can be achieved with a continuous probe beam combined with heterodyne detection. Indeed, a 50 cm delay line only provides few ns time delays (see Section 2.2), while in principle with a continuous probe one can obtain time delays between few ns and infinite. The lower limit depends on how fast is the detector response.

1.3 Magnetization dynamics

The aim of the thesis is to study the TG-induced magnetization dynamics in a ferromagnetic thin film. In this section it will be shown that, due to magnetoelastic coupling, a spin wave with wavelength Λ is excited. Furthermore, it will be explained why we are sensitive to the thin film FMR when an external magnetic field is applied. To start with, a brief introduction on magnetization dynamics is given.

Below the Curie temperature, ferromagnetic materials exhibit a spontaneous ordering of the atomic magnetic moments. The resulting macroscopic magnetization is defined as $\vec{M} = \vec{m}/V$ where V is the volume containing the magnetic moment $\vec{m}$. Assuming that $\vec{M}$ remains constant in magnitude, its motion in an external magnetic field can be described by the Landau–Lifshitz–Gilbert equation [9]

$$\frac{\mathrm{d}\vec{M}}{\mathrm{d}t} = -\gamma[\vec{M} \times \vec{H}] + \frac{\alpha}{M}\left[\vec{M} \times \frac{\mathrm{d}\vec{M}}{\mathrm{d}t}\right] \tag{1.8}$$

where γ is the gyromagnetic ratio, $\alpha > 0$ the damping parameter and $\vec{H}$ the external magnetic field. The first term is the torque $\vec{\tau}$ exerted on the magnetic moment by the magnetic field and it is responsible for the Larmor precession of $\vec{M}$ about $\vec{H}$ an with an angular frequency $\omega_l = \gamma H$. The second term is the damping torque $\vec{\tau}_d$ and

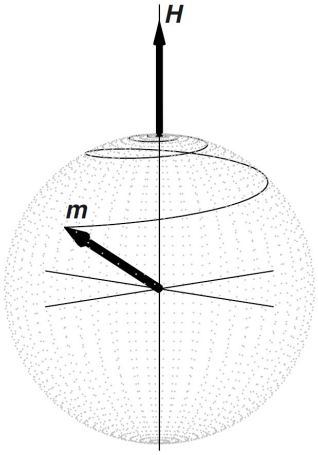

Figura 1.8: Precessional motion of the magnetic moment $\vec{m}$ according to the Landau–Lifshitz–Gilbert equation with a damping parameter $\alpha > 0$. $\vec{m}$ precesses about the external magnetic field while the damping torque tends to align it in the magnetic field direction, which corresponds to equilibrium. Image from [9].

decribes the magnetization damping, a dissipative phenomena that tends to align the magnetization with the external field. Therefore, the magnetization precesses around the external magnetic field until it aligns with it. When this happens, equilibrium is reached and the sample is macroscopically magnetized.

1.3.1 Ferromagnetic resonance

Historically, the dynamics associated with the motion of a the magnetization $\vec{M}$ in an external magnetic field has been thoroughly studied by FMR [9]. Figure 1.9 shows a typical FMR experiment. As mentioned before, when a strong static field $\vec{H}||\hat{z}$ is applied, $\vec{m}$ starts to precess around it with the Larmor frequency ω_l. A weaker frequency-dependent field $\vec{H}'$, that rotates in a plane perpendicular to $\vec{H}$, exerts a torque $\vec{\tau}'$ and supplies the energy so that it causes θ to increase. The condition for keeping θ constant, and so reaching resonance is that $\vec{M}$ and $\vec{H}'$ rotate together at the Larmor frequency. Therefore, when this happens $\vec{\tau}' = -\vec{\tau}_d$. In the case of the electron spin, appropriate frequencies of the rotating magnetic field are generated by establishing a standing electromagnetic (EM) wave with a wavelength λ of a few cm in a cavity. Since $c = \lambda\nu = 3 \cdot 10^8$ ms^{-1} this correspond to the GHz frequency range. The sample is placed in an antinode of the EM wave and the magnitude of the static field $\vec{H}$ is changed until a maximum absorption of energy occurs from the microwave cavity, which means that the Larmor frequency matches the EM standing wave. When this happens, the energy absorbed from the microwave cavity exactly compensates the energy loss from the damping of the precession in the material.

Therefore, FMR is a powerful technique that allows to measure many important properties of magnetic media, from bulk to nano-scale magnetic thin films. For example, it has been used to measure the Curie temperature [42], total magnetic moment [43] and the magnetization damping mechanism [44]. Furthermore, FMR

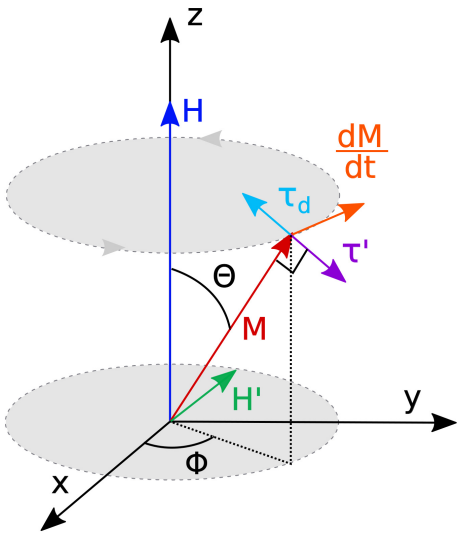

Figura 1.9: Fields and torques in magnetic resonance for the case of an electron spin [9]. According to the right hand rule, the static external field $\vec{H}$ causes the magnetic moment precession about $\hat{z}$ with $\mathrm{d}\vec{M}/\mathrm{d}t$ parallel to the xy plane. The weaker rotating field $\vec{H}'$ is applied perpendicular to $\vec{H}$, so that is parallel to the xy plane and it exerts a torque $\vec{\tau}'$ perpendicular to $\vec{M}$. The effect of $\vec{H}'$ is therefore to increase the angle θ between $\hat{z}$ and $\vec{M}$, against the precessional damping that tends to $\vec{M}$ along $\vec{H}$. Changing the magnitude of $\vec{H}$, FMR resonance is reached when there is a maximum absorption of energy from the microwave field $\vec{H}$; when this happens, θ remains constant. Adapted from [9].

can also be used to investigate complex phenomena such as spin pumping, the spin hall effect and the inverse spin hall effect [45, 46, 47].

The FMR signal is affected by the external magnetic field direction and by the shape of the sample. In the case of a thin ferromagnetic film with an in-plane external magnetic field, Kittel proved [10] that the FMR resonance is reached when

$$f_K = \gamma\mu_0\sqrt{H_0(H_0 + M_s)} \tag{1.9}$$

where μ_0 is the vacuum magnetic permeability, M_s is the saturation magnetization of the sample and H_0 is the magnetostatic field. In general, in ferromagnetic thin films it is the sum of the applied external field and an effective fields given by different energy contributions (see Section 1.3.2). Therefore, the Kittel formula predicts a $f_K \neq 0$ even when there is no external field.

1.3.2 Phonon-driven magnetization dynamics

As mentioned in the previous section, when an external field is applied the magnetic moments of a ferromagnetic material tend to align in its direction. In magnetostrictive materials this causes lattice deformations, resulting in variations in the sample structural anisotropy. Most ferromagnetic materials exhibit some measurable magnetostriction [48]. In this thesis work we are interested in its reciprocal effect, the so-called inverse magnetostriction. It consists in variations of the magnetization due to the presence of strains in the ferromagnetic material.

Let's see how a dynamic strain ε affects the magnetization based on inverse magnetostriction effect [3, 49, 5, 4]. Figure 1.10 depicts the case of interest. From the macrospin approximation, the static magnetization $\vec{M}$ of the ferromagnetic thin film is assumed to be spatially uniform and equal to the saturation value M_s. Its direction is determined by the in-plane applied external field $\vec{H}$. The TG launches stationary acoustic waves with a specific wave vector $\vec{q} \,||\, \hat{x}$, related to the TG pitch Λ.

When dealing with polycrystalline ferromagnetic thin film, the magnetization dynamics is described by the generalized Landau–Lifshitz–Gilbert equation, which can be easily obtained from Equation 1.8 by replacing $\vec{H}$ with an effective field $\vec{H}_{eff}$. It is in general time dependent and can be expressed as

$$\vec{H}_{eff}(t) = -\frac{1}{\mu_0}\frac{\mathrm{d}U(t)}{\mathrm{d}\vec{M}} \tag{1.10}$$

where $U(t)$ is the free energy.

The total free energy density of a ferromagnet is given by

$$F = U/V = F_0 + F_{me} \tag{1.11}$$

where F_0 and F_{me} are respectively the magnetostatic and magnetoelastic contributions.

The magnetostatic free energy density can be expressed as

$$F_0 = F_{ex} + F_z + F_k + F_d \tag{1.12}$$

where F_{ex} is the exchange energy, F_z the Zeeman energy density, F_k the magnetocrystalline anisotropy and F_d is the demagnetization energy density.
The exchange coupling energy, which is due to the interaction between atomic spins, can be expressed as

$$F_{ex} = -\mu_o \vec{H}_{ex} \cdot \vec{M} \tag{1.13}$$

where μ_0 is the vacuum magnetic permeability and $\vec{H}_{ex}$ is the exchange field. In case of homogeneous materials, the contribution to $\vec{H}_{ex}$ due to the strain-induced

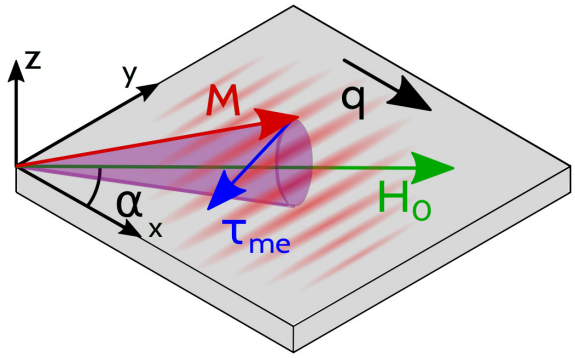

Figura 1.10: Schematic representation of the TG-induced magnetization dynamics. The in-plane thin film magnetization is driven out of plane by the magnetoelastic torque $\vec{\tau}_{me}$

anisotropies can be calculated as

$$\vec{H}_{ex} = \frac{D_{ex}}{\mu_0}\nabla^2\vec{M} \tag{1.14}$$

where D_{ex} is the exchange stiffness.
Given an external magnetic field, the Zeeman energy density is

$$F_z = -\mu_0\vec{H}\cdot\vec{M} \tag{1.15}$$

The magnetocrystalline anisotropy F_k can be instead expressed as

$$F_k = B_u(\vec{u}\cdot\vec{M})^2 \tag{1.16}$$

where B_u is an uniaxial in plane anisotropy along $\vec{u}$. As in a policrystalline thin film this term is relatively small respect to other contributions, it will be neglected.
Finally, the demagnetization energy is given by

$$F_d = B_d M_\perp^2 = B_d M_z^2 \tag{1.17}$$

where M_z is the out of plane magnetization component, B_d is the anisotropy field along the film normal. For a policristallyne thin film the main contribution of F_d is the demagnetization field $\mu_0 M_s/2$.
The competition of these different energy terms gives the magnetic ground state. In the case of interest, it is dictated by the demagnetization energy contribution, resulting in an in-plane magnetization pointing in the same direction of the in-plain external magnetic field $\vec{H}$.

The magnetoelastic contibution F_{me}, which takes into account the interaction of the strain with the magnetization, can be expressed as [3]

$$F_{me} = \frac{B_1}{M_s^2}\sum_i M_{ii}^2\epsilon_{ii} + \frac{B_2}{M_s^2}\sum_i\sum_{j\neq i} M_i M_j \epsilon_{ij} \tag{1.18}$$

where B_1 and B_2 are the magnetoelastic constants, M_i is the i-th magnetization vector component, and ϵ_{ij} are the strain tensor components. The magnetization equilibrium is achieved when the magnetization is aligned along the $\vec{H}_{eff}$ direction, that is where F is minimum. In the case of a static strain, the competition of the different energy densities results in in-plane energy minima, which correspond to just as many preferred magnetization orientations.

As with the TG technique we are able to excite the RSAW and the SSLW, the sums in Equation 1.18 reduce to only few terms. If we arbitrarily assume that these two waves propagate in the $\hat{x}$ direction, the non-zero strain components for the RSAW are ε_{xx}, ε_{xz} and ε_{zz}, while for the SSLW ε_{xx} is the only active one. However, it is known [49] that ε_{xx} prevails in the near-surface region, which for our purposes can be considered the only non zero strain component. A more complete dissertation is reported in Reference [5].

The magnetoelastic coupling strength, can be estimated by the elastically driven torque $\vec{\tau}_{me}$ acting on the in-plane thin film magnetization. Considering

$$\varepsilon_{xx}(x,t) = \varepsilon_{xx}^{TOT}(x,t) = \varepsilon_{xx}^{RSAW}(x,t) + \varepsilon_{xx}^{SSLW}(x,t) \tag{1.19}$$

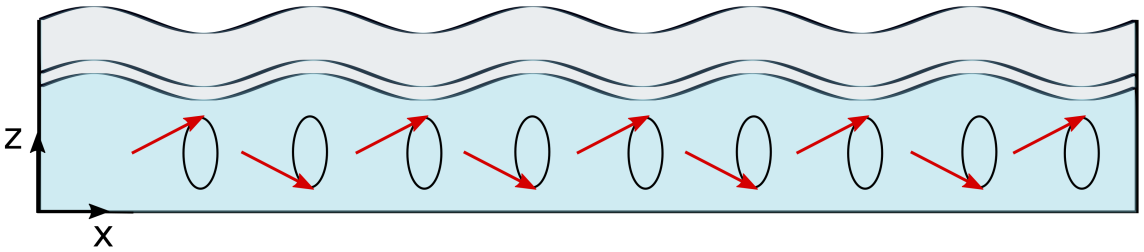

Figura 1.11: Schematic representation of a SAW propagating in the sample. The SAW acts as a driving force of a spin wave of equal wavelength due to inverse magnetostrictive effect.

as the only active strain component the only non zero term, Equation 1.18 becomes

$$F_{me}(x,t) = B_1 \frac{M_x^2}{M_s^2} \varepsilon_{xx}(x,t) \tag{1.20}$$

which gives an magnetoelastic effective field

$$\vec{H}_{me}(x,t) = -\frac{\mathrm{d}F_{me}}{\mathrm{d}\vec{M}} = -\hat{x}\left[2B_1 \frac{M_x}{M_s^2} \varepsilon_{xx}(x,t)\right] \tag{1.21}$$

The in-plane magnetization of the thin film is

$$\vec{M} = M_x\ \hat{x} + M_y\ \hat{y} = M\cos\alpha\ \hat{x} + M\sin\alpha\ \hat{y} \tag{1.22}$$

Consequently, the magnetoelastic torque $\vec{\tau}_{me}$ can be written as

$$\begin{aligned} \vec{\tau}_{me}(x,t) = \frac{\mathrm{d}\vec{M}}{\mathrm{d}t} &= -\gamma\mu_0\left[\vec{M} \times \vec{H}_{me}(x,t)\right] = \\ &= -\hat{z}\left[2\mu_o\gamma \frac{B_1}{M_s^2} M_x M_y \varepsilon_{xx}(x,t)\right] = \\ &= -\hat{z}\left[\mu_o\gamma B_1 \frac{M^2}{M_s^2} \sin(2\alpha)\varepsilon_{xx}(x,t)\right] \end{aligned} \tag{1.23}$$

where α is the angle between $\vec{M}$ and $\vec{H}$.

Equation 1.23 shows that the elastically driven torque depends on the angle α through a four-fold symmetry. Indeed, is maximum at $\alpha = 45°$, $135°$, $225°$ and $315°$, while it is zero at $\alpha = 0$ and $\alpha = 90°$. Furthermore, its spatial and temporal modulation is dictated by $\varepsilon_{xx}(x,t)$.

At a given time $t = t_0$ in the compressional regions ($\varepsilon_{xx} < 0$) $\vec{\tau}_{me}$ is directed as $\hat{z}$ and it tilts the magnetization out of plane, resulting in an out-of-plane component $M_z > 0$. Similarly, where the strain is tensional ($\varepsilon_{xx} > 0$), the magnetization has an out-of-plane component $M_z < 0$. Figure 1.11 depicts the resulting phase shift in the magnetization precession about $\vec{H}_0$ along $\hat{x}$. When passing from a compressive to tensional strain maxima, the phase shift is π. Therefore, the SAWs pump a spin wave with equal wavelength. Spin wave resonance is observed when there is an external magnetic field and $\vec{M}$ precesses due to $\vec{\tau}_{me}$ at the Kittel frequency f_K.

Elastically driven FMR

FMR can be achieved not only by microwave photons, but also by microwave phonons. Elastically driven FMR in ferromagnetic thin films has been experimentally proved with different techniques exploiting SAWs. In most cases SAWs are generated by IDTs [4]. However, the TG it is extremely suitable and equally effective technique, since it allows to generate coherent phonons with a tunable $\vec{q}$.

As mentioned in Section 1.3.1, the most common approach is to reach FMR resonance applying the rotating RF magnetic field $\vec{H}'$. In this case we can therefore express

$$\vec{H}_{eff}(t) = \vec{H}_0 + \vec{H}'(t) \tag{1.24}$$

where $\vec{H}_0$ is the magnetostatic contribution.

Unlike conventional FMR, SAW-driven FMR arises from the internal RF $\vec{H}_{me}$ rather than the external RF magnetic field $\vec{H}'$. Indeed, a radio-frequency surface acoustic wave generates a strain $\epsilon = \epsilon(\vec{x}, t)$, which in turns gives a $F_{mel} = F_{mel}(\vec{x}, t)$ and so $\vec{H}_{eff}$ turns out to be

$$\vec{H}_{eff}(\vec{x}, t) = \vec{H}_0 + \vec{H}_{me}(\vec{x}, t) \tag{1.25}$$

A fundamental difference between photon-diven and phonon-driven FMR, is that while $\vec{H}'$ is a real, externally applied magnetic field, $\vec{H}_{me}$ is an internal, virtual anisotropy field due to magnetoelastic interaction. This spin-mechanical interaction prevails at radio frequencies so that magnonic and phononic degrees of freedom become strongly coupled [50]. Furthermore, the effective field $\vec{H}_{me}$ itself is a function of both strain ε and magnetization $\vec{M}$. Hence, in phonon-driven FMR, the driving field $\vec{H}_{mel}$ itself already derives from a phonon-magnon coupling [50, 5]. Depending on the type of SAWs generated in the ferromagnet, several strain components with different amplitudes may superimpose, resulting in a non-trivial and complex phonon-driven FMR signal. In general the resulting $\vec{H}_{eff}$ is not orthogonal to the external magnetic field, unlike what happens in conventional FMR. The phonon-driven FMR has also been proved to be several orders of magnitude more efficient with respect to the conventional one [51]. Figure 1.12 qualitatively depicts the magnetization precession around the effective magnetic field $\vec{H}_{eff}$, the photon-driven FMR and the phonon-driven FMR.

What is measured?

Since the focal spot of our probe is much larger than the acoustic (and spin) wavelength, we measure the *average* out-of-plane magnetization M_z. As M_z has the same periodicity of the acoustic waves, the out-of-plane magnetization profile can be described as [6]

$$M_z(x, t) = A\cos(qx)\mathrm{e}^{i\omega t} \tag{1.26}$$

Therefore, $< M_z(t) >= 0$ over a period of the SAWs.

However, the TG excitation not only induces a spin wave, but also builds a temperature profile $T(x)$ with same spatial periodicity as the SAWs. In particular, the

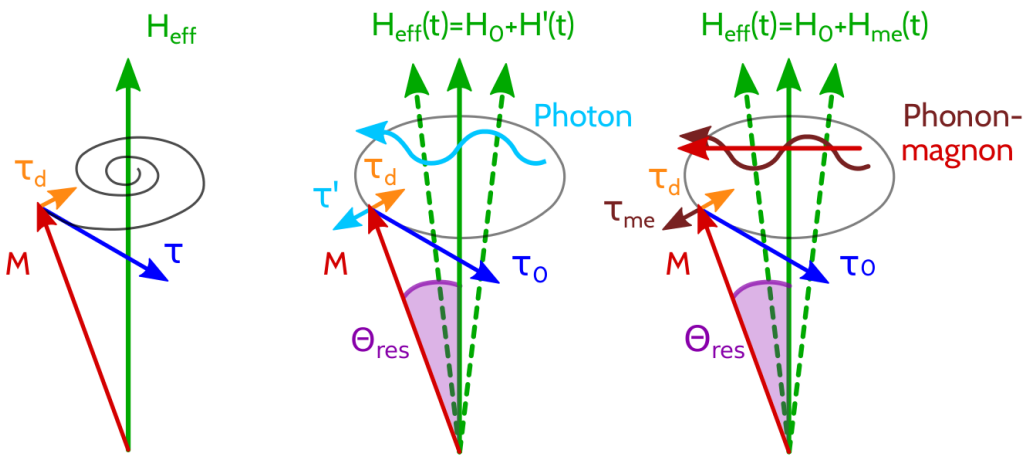

Figura 1.12: The magnetization $\vec{M}$ precesses around the effective magnetic field $\vec{H}_{eff}$ (left panel). Photon-driven ferromagnetic resonance (central panel). Phonon-driven ferromagnetic resonance (right panel). Adapted from [50].

temperature, the tensional strain and the pump interference maxima coincide. As described by the Curie-Weiss law, the saturation magnetization at a certain temperature $M_s(T)$ decreases as T is increased. It follows that in the pump interference maxima, where the temperature is higher, $M_z(x,t)$ is lower than in the minima. The combined effect of the magnetostatic wave and the temperature profile can be written for the out of plane component as

$$M_z(x,t) = A\frac{M_s(T(x))}{M_s(0)}\cos(kq)e^{-i\omega t} \tag{1.27}$$

where A is the precessional amplitude of the TG-induced magnetostatic wave. The net out-of-plane magnetization component is given by the integral over a spatial period $\Lambda = 2\pi/q$ of $M_z(t)$. Combining both the temperature and magnetostatic wave profile is

$$< M_z(t) >= Ae^{-i\omega t}\int_0^{\Lambda}\frac{M_s(T(x))}{M_s(0)}\cos(qx)\mathrm{d}x, \tag{1.28}$$

which gives an $< M_z(t) >\neq 0$. Figure 1.13 qualitatively depicts the temperature and M_z profiles respect to ε_{xx}. Therefore, we are able to resolve only the magnetization dynamics in several acoustic wave semiperiods.

Over a spatial extension $\Lambda/2$, the magnetic moments accumulates a π phase shift. Furthermore, when there is an external field $\vec{H}$, they also precess with a constant relative phase at the Kittel frequency f_K. When $\vec{H}_{me}(x,t)$ rotates because of $\varepsilon_{xx}(x,t)$ with a frequency f_K, a resonance is observed. Specifically, this happens when the frequency of the acoustic waves matches the Kittel frequency f_K.

As mentioned earlier, the Kittel formula 1.9 gives the FMR precessional frequency of the thin film moments in an external magnetic field. Therefore, in an infinite ideal thin film and when there is no TG-induced magnetoelastic coupling, the magnetic moments in an external magnetic field $\vec{H}$ precess in phase with frequency f_K. This collective motion is the so-called Kittel mode, a spin wave with $\vec{k} = 0$. However, as

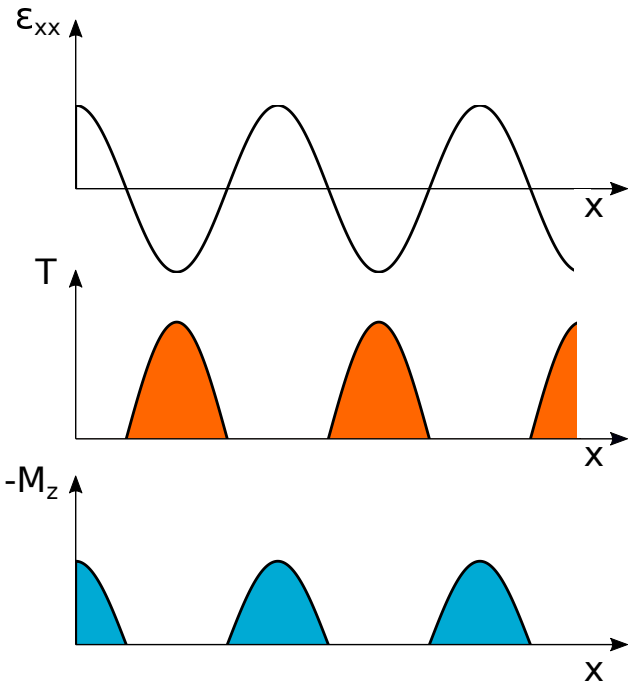

Figura 1.13: Qualitative sketch of temperature and M_z profiles with respect to ε_{xx}. Simulation about the temperature profile evolution are reported in Reference [6, 52]. In the regions where the pumps constructively interfere, the temperature locally increase. On the contrary, M_z decreases in the interference minima, resulting in a non-zero $< M_z >$.

mentioned before, the TG, through magnetoelastic effect, generates a spin wave with periodicity Λ but we only able to detect the magnetization dynamics in the "cold" TG interference fringes. At resonance, the magnetic moments within a semiperiod precess with a well defined phase, which is constant over time. This same dynamics repeats itself in every "cold" region. We are therefore able to probe the collective dynamics of magnetic moments precessing with a well defined phase relation in several "cold" interference fringes. In this sense, we observe the acoustically driven FMR.

1.4 Time resolved Faraday probe

Magneto-optical probes are often used to study magnetic properties of materials in a contactless and non-invasive way. The Faraday effect consists in a change of the polarization of the incident beam upon transmission through a magnetic material. It is similar to the Magneto Optical Kerr Effect (MOKE), with the only difference that the variations in polarization are observed in the transmitted beam rather than in the reflected one. Experimentally, the transmission geometry is easier to implement but it requires the sample to be transparent.

Depending on the relative orientation of the wave vector $\vec{k}$ of the incident beam and the sample magnetization $\vec{M}$ one can distinguish between Faraday or Voigt configuration. The former is when $\vec{M} \parallel \vec{k}$, while the latter has $\vec{M} \perp \vec{k}$. Both configurations probe the magnetization component along $\vec{k}$. However, while the

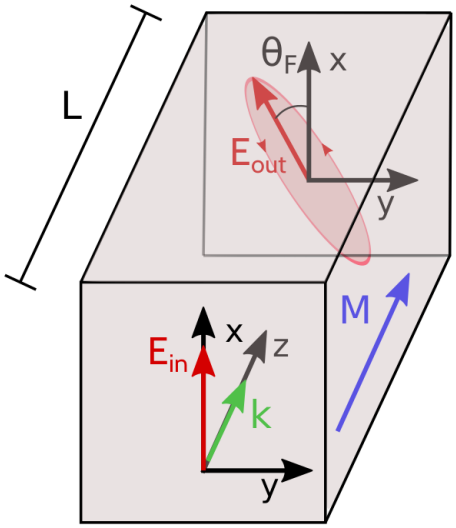

Figura 1.14: Illustration of the Faraday configuration. The state of the polarization of the incident light is rotated by Θ_F upon propagation in a magnetic medium.

Faraday effect is linear in the magnetization along $\vec{k}$, it can be shown analitically that the Voigt is a second order effect [53]

In the specific case, we have $\vec{k} \perp \vec{M}$, since the magnetization is in plane and we use a normal incidence probe. However, as we are interested in probing the TG-induced out-of-plane magnetization dynamics $M_z(t)$ $||$ $\vec{k}$ and the Voigt effect is negligible [54], the Faraday configuration must be taken into account.

Let us consider a linearly polarized light beam with $\vec{k}$ $||\vec{M}$ and propagating along $\hat{z}$, as shown in Figure 1.14. Let us assume the incident light polarization along $\vec{x}$ for $z < 0$. It can be written as the combination of left $(+\sigma)$ and right $(-\sigma)$ circularly polarized light as

$$\vec{E}(z,t) = E_0 e^{i(kz-\omega t)}\hat{x} = \frac{E_0}{2}(\hat{x} + i\hat{y})e^{i(kz-\omega t)} + \frac{E_0}{2}(\hat{x} - i\hat{y})e^{i(kz-\omega t)} \tag{1.29}$$

The electric field propagating inside the material can be written as

$$\vec{E}(z,t) = \frac{E_0}{2}(\hat{x} + i\hat{y})e^{i(\frac{2\pi n_+}{\lambda}z-i\omega t)} + \frac{E_0}{2}(\hat{x} - i\hat{y})e^{i(\frac{2\pi n_-}{\lambda}z-i\omega t)} \tag{1.30}$$

where n_+ and n_- are respectively the refractive indices for left and right polarized light and λ is the the incident light wavelength in vacuum. After some trigonometric manipulation [55], Equation 1.30 can be rewritten as

$$\vec{E}(z,t) = \frac{E_0}{2}e^{i(\frac{2\pi\bar{n}}{\lambda}z-i\omega t)}\left(\hat{x}\cos\frac{\delta}{2} + \hat{y}\sin\frac{\delta}{2}\right) \tag{1.31}$$

where

$$\bar{n} = \frac{n_+ + n_-}{2} \qquad \text{and} \qquad \delta = \frac{2\pi z(n_+ - n_-)}{\lambda} \tag{1.32}$$

If for the moment we neglect absorption and thus we consider n_+ and n_- as real, δ is the phase shift between left and right component due to the birefringence of

the magnetic medium. Equation 1.31 describes a linearly polarized wave with a polarization rotated of $\delta/2$ from $\hat{x}$ to $\hat{y}$. Therefore, when there is no absorption the Faraday rotation can be expressed as

$$\Theta_F = \frac{\delta}{2} = \frac{\pi(n_+ - n_-)L}{\lambda} \tag{1.33}$$

where L is the distance travelled in the medium.

When also absorption needs to be included, the complex refractive indices need must be taken into account. As the Maxwell equations describe the optical properties of the materials, they are the starting point to derive the complex n_+ and n_-. The needed Maxwell's equations are

$$\vec{\nabla} \times \vec{E} = -\frac{\partial \vec{B}}{\partial t} \tag{1.34}$$

and

$$\vec{\nabla} \times \vec{H} = \epsilon_0 \frac{\partial \vec{E}}{\partial t} + \vec{J} \tag{1.35}$$

where $\mu_0 \vec{H} = \vec{B} - \mu_0 \vec{M}$ and

$$\vec{J} = \epsilon_0 \frac{\partial \vec{P}}{\partial t} + \vec{\nabla} \times \vec{M} = \epsilon_0 \bar{\bar{\chi}} \frac{\partial \vec{E}}{\partial t} + \vec{\nabla} \times \vec{M} \tag{1.36}$$

$\bar{\bar{\chi}}$ is the electric susceptibility tensor and $\vec{J}$ takes into account the polarization, magnetization and free carriers currents. Equation 1.35 can be express as

$$\vec{\nabla} \times \vec{H} = \frac{\partial \vec{D}}{\partial t} \tag{1.37}$$

where

$$\vec{D} = \epsilon_0 \vec{E} + \vec{P} = \epsilon_0 \bar{\bar{\epsilon}}_r \vec{E} \qquad \text{and} \qquad \bar{\bar{\epsilon}}_r = 1 + \bar{\bar{\chi}} \tag{1.38}$$

$\bar{\bar{\epsilon}}_r$ is the dielectric tensor and depends on the magnetic state of the material and the magneto-optical effects can be traced back to its tensorial nature. If the magnetization varies slowly with respect to λ, combining Equations 1.34 and 1.38 we get

$$\vec{\nabla}^2 \vec{E} - \nabla(\vec{\nabla} \cdot \vec{E}) = \mu_0 \epsilon_0 \bar{\bar{\epsilon}}_r \frac{\partial^2 \vec{E}}{\partial t^2} \tag{1.39}$$

Looking for plane wave solutions we obtain

$$n^2 \vec{E} - \vec{n}(\vec{n} \cdot \vec{E}) = \bar{\bar{\epsilon}}_r \vec{E} \tag{1.40}$$

where $\vec{n} = \frac{w}{c}\vec{k}$ is the complex refractive index. Since electromagnetic waves have $\vec{E} \perp \vec{k}$, Equation 1.40 reduces to

$$n^2 \vec{E} = \bar{\bar{\epsilon}}_r \vec{E} \tag{1.41}$$

In the case of a cubic crystal and when only $M_z \neq 0$ [53]

$$\bar{\bar{\epsilon}}_r = \epsilon \begin{pmatrix} 1 & -iQM_z & 0 \\ iQM_z & 1 & 0 \\ 0 & 0 & 1 \end{pmatrix} \tag{1.42}$$

where Q is the Voigt constant of the material, which is proportional to the saturation magnetization. The dielectric tensor plays a role in the electronic transition of electrons in the valence band, since the off-diagonal elements determine different absorption rates the for left and right circular polarized light. Combining Equation 1.41 with 1.42, it can be derived that

$$n_{\pm}^2 = (1 \pm QM_z) \tag{1.43}$$

Furthermore, the eigenvalues of Equation 1.41 are $\vec{E} = E_0(\hat{x} \pm i\hat{y})$, which are the left and right circularly polarized light components. Assuming Q being small, in first approximation Equation 1.43 becomes $n_{\pm} = \sqrt{\epsilon}(1 \pm \frac{QM_z}{2})$. The Faraday rotation can therefore be explicitely written as

$$\Theta_F = \pi \frac{L}{\lambda} \Re(\sqrt{\epsilon} Q M_z) \tag{1.44}$$

In the more general case where both circular birefringence and dichroism are present, the Faraday rotation can also be expressed as

$$\Theta_F = LVM_z \tag{1.45}$$

where V is the Verdet constant, which generally depends on the wavelength and temperature.

In order to detect the magnetoelastic coupling, we implemented in the TG experimental setup a time resolved Faraday probe. This allows to follow the dynamics of the TG-induced out-of-plane magnetization precession, since $M_z(t)$ is straightforwardly probed by measuring the Faraday rotation $\Theta_F(t)$.

Some considerations on the expected Faraday signal can be made.
When reversing the applied magnetic field the in-plane magnetization changes sign, which means $\vec{M} \rightarrow -\vec{M}$. However, Equation 1.23 shows that $\tau_{me} \propto M^2$, and so it is invariant for $\vec{H} \rightarrow -\vec{H}$. The magnetic response of the system is therefore expected to depend only on the magnetic field magnitude. In addition to this, τ_{me} shows a four-fold symmetry, therefore no Faraday signal is expected for $\alpha = 0, 90°$.

As mentioned in Section 1.3.2, the temperature plays a crucial role in the magnetic detection. The pump fluence need to be carefully calibrated: on one hand, it needs to be enough to launch the SAWs in the substrate and provide an appropriate magnetic contrast, on the other, the sample surface must be preserved.

Capitolo 2

Experimental procedures

2.1 PHAROS laser source

The source is a Yb:KGW-based integrated femtosecond laser system (PHAROS, Light Conversion), characterized by a turn-key operation and by high pulse-to-pulse stability. The system produces 300 fs pulses at 1030 nm with a tunable repetition rate from single-shot to 1 MHz. The average power is 20 W above 50 kHz. The maximal energy-per-pulse, equal to 400 µJ, is available in the $0 - 50$ kHz interval instead. Above these values, the energy per pulse is determined by the selected repetition rate setting: 200 µJ/pulse at 100 kHz, 100 µJ/pulse at 200 kHz, and 20 µJ/pulse at 1 MHz. Once the fundamental repetition rate is set, the corresponding energy/pulse is provided. From this condition a lower repetition rate can be set by pulse-picking of the pulses; this possibility preserves the energy/pulse and is particularly useful for the optimization of non-linear optical processes since the same peak power is available but with a reduced thermal load. The tunable repetition rate has direct consequences on experiments, allowing us to find the ideal compromise between (probe) signal statistics and (pump-induced) sample heating.

2.2 Pulsed TG setup

This section describes the optical setup we built to perform TG measurements in both reflection and transmission geometry. A picture of the optical table is shown in Figure 2.1, while Figure 2.2 depicts a sketch of the TG experimental setup.

Infrared pump pulses at 1030 nm wavelength and with temporal length of 300 fs are produced by the rigenerative amplifier of the PHAROS laser source. As the average power is 20 W, 10% of its output is enough to run our experiment. This allows to work in a parasitic way when the PHAROS is simultaneously used as laser source in some other experiments.

The beam is then split again by a 70/30 beamsplitter: 70% is used for the pump while the remaining 30% passes through a Beta-Barium Borate (BBO) crystal properly oriented to get the phase matching condition and to obtain Second Harmonic

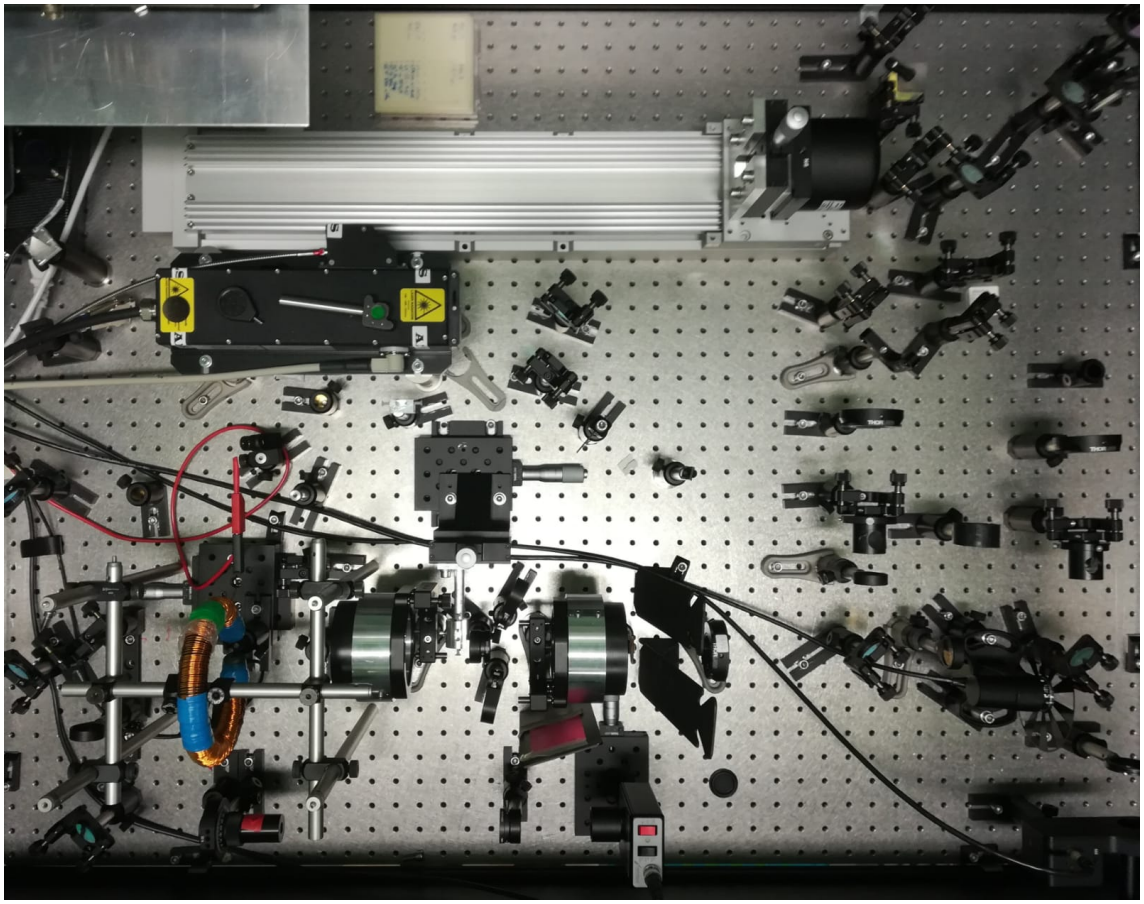

Figura 2.1: Picture of the optical table.

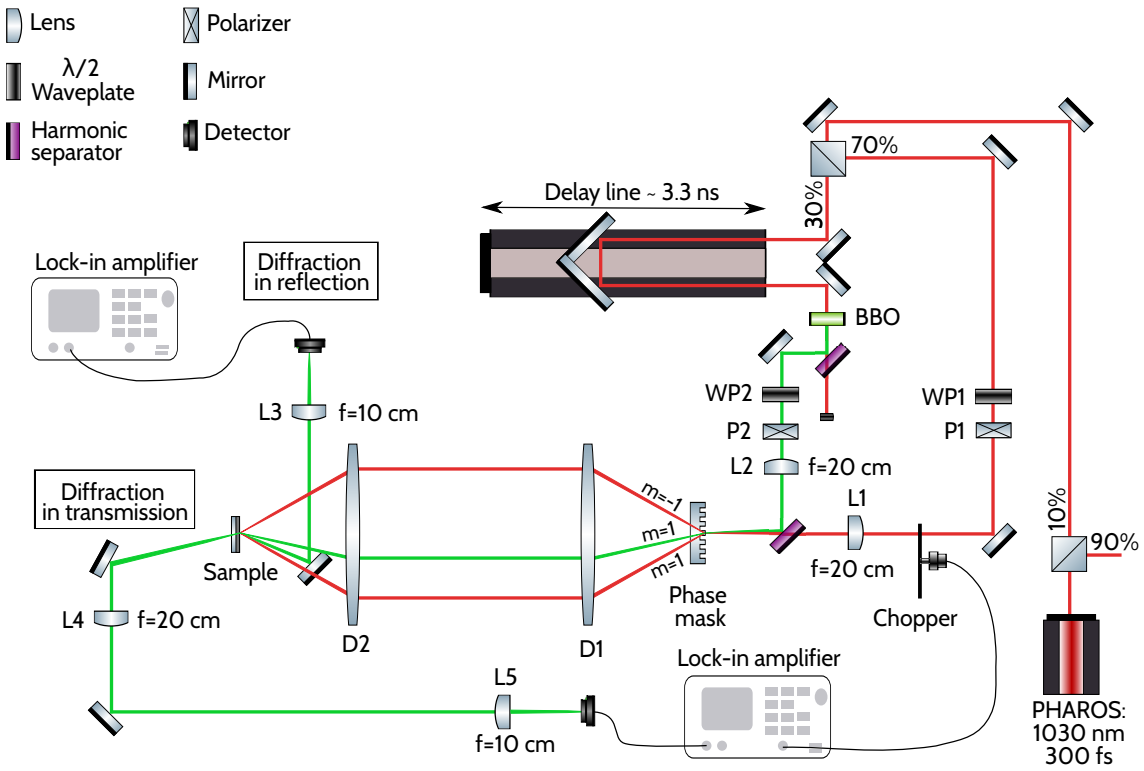

Figura 2.2: Pulsed TG setup scheme in reflection and transmission geometry. The laser source is the PHAROS, which generates 300 fs pulses at 1030 nm. Just 10% of its output is actually used. A second beamsplitter splits the beam again and the 30% of it passes through the delay line and across the BBO crystal. The harmonic separator provides a pulsed probe with a wavelength of 515 nm. Attenuation of the two beam is possible thanks to the waveplates (W1, W2) and the polarizers (P1, P2) placed on each branch. Both pump and probe are then focalized with plano-convex lenses (L1, L2) on the phase mask and diffracted. Two identical doublets (D1, D2) in confocal configuration recombine them. One of the first orders of the 515 nm is used as the probe. The pump consists in the two first diffraction orders of the 1030 nm, which interfere on sample generating the TG. Acoustic modes can be directly characterized by measuring the intensity of the probe beam, partially diffracted by the induced grating at the phase matching angle. The TG signal is finally focalized by a plano convex lens into a femtowatt photoreceiver and amplified by the lock-in. In reflection geometry the sample has to be tilted downwards, otherwise for the phase matching condition the diffracted beam is superimposed on the incident probe. For illustrative purposes it is drawn at a different angle. In transmission geometry the sample surface is set orthogonal to the scattering plane.

Generation (SHG). The harmonics are then divided by an harmonic separator, which reflects only the second harmonic (515 nm).

In order to finely tune the fluence on sample, a $\lambda/2$ waveplate followed by a polarizer is placed along both the pump (WP1, P1) and probe (WP2, P2) branches. Indeed, when linearly polarized light pass throughout a $\lambda/2$ waveplate that has its fast axis at an angle θ with respect to the polarization of the incident light, it rotates the polarization plane of 2θ. The polarizers are set so that, if the light polarization is rotated by the $\lambda/2$ waveplate, only the vertical component passes across the polarizer. Consequenty, as the PHAROS output is horizontally polarized, the fluence on sample can be reduced by conveniently rotating the $\lambda/2$ waveplates.

Pump and probe are collinearly coupled by the harmonic separator and focalized on a phase mask by plano-convex lenses (L1, L2) with focal length $f = 20$ cm. Upon diffraction by the phase mask, the diffraction maxima are recombined by the doublets (D1, D2) in a confocal configuration. The first diffraction orders of the 1030 nm are used as the pump, while the probe consists in one of the first diffraction orders of the 515 nm. All other diffraction orders are stopped by a beam blocker. The experimental advantages of this configuration as well as the doublets and phase mask features will be discussed in Section 2.5.

The phase mask was placed in the focus of L1 and L2 by using the so-called razor blade method. It consists in mounting a razor blade on two horizontal micrometric translators and cutting the laser beam sideways in the expected focus region. If the blade is just before or after the focus position, when the razor blade intercepts the laser spot on the reference sheet starts disappearing from one side; if, on the other hand, the blade is placed in the focus position, the spot intensity decreases gradually as the blade penetrates into the beam. Figure 2.3 illustrates this procedure in the case of the 515 nm. This method was also used to probe the focus depth. The 1030 and 515 nm waists turned out to be spatially coincident and ~ 5 cm long. The phase mask is placed in the middle of this region.

In order to perform time resolved measurements, it is necessary to introduce a time delay between pump and probe. This is accomplished using a 50 cm long delay stage. The maximum achievable time delay can be easily calculated as

$$t^{\text{delay}} = \frac{2L}{c} = 3.33 \text{ ns} \tag{2.1}$$

where L is the delay line length and c the speed of light in air.

To check the correct overall alignment, a Third Harmonic Generation (THG) crystal was placed in the focus position. From now on with focus is meant the point where the second doublet recombines the three beams of interest in its focal plane. Indeed, THG from a pump and probe pulses takes place only if these two are both spatially and temporally overlapped and the crystal is properly oriented to satisfy the phase matching condition. Therefore, the generation of the third harmonic from a THG crystal placed in the sample position guarantees an overall good alignment, which is critical to observe the TG signal.

As discussed in Section 1.2, the grating generated on the sample causes a fraction of the probe beam to be diffracted, both in transmission and in reflection. By measuring the modulation of its intensity, it is possible to study the dynamics induced

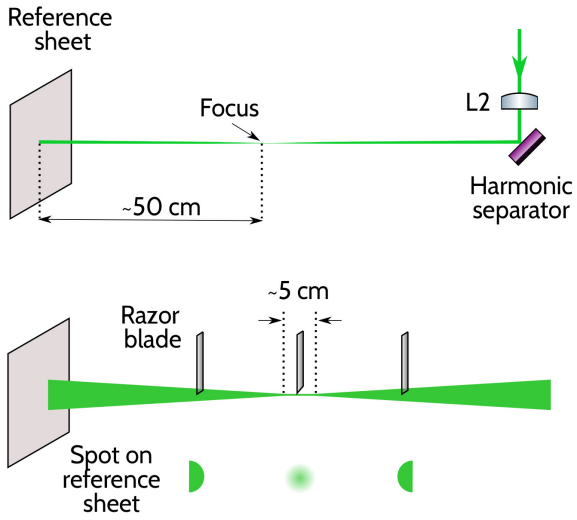

Figura 2.3: Razor blade method to find focus position of L2. Before aligning the doublets, a reference sheet was placed about 50 cm away from the expected focus position (top panel). Using a razor blade mounted on two coupled micrometric translators, the laser beam is cut at different positions. Before and after the focus position the spot on the reference sheet starts disappearing from one side when the razor blade intercepts the laser beam. For the entire focus depth, when the laser blade cuts the laser beam the spot loses its intensity homogeneously and its shape is not affected (bottom panel). This method was also used find the focus position of L1. The measured focus depth is ~ 5 cm for both the pump and probe beams.

by TG in the sample as a function of the time delay between pump and probe. When performing a TG measurement in the reflection geometry the sample normal has to be slightly tilted with respect to the probe incidence direction. This is necessary because otherwise, due to the phase matching condition described in Section 1.2, the scattered beam would be exactly overlapped to the probe beam, which would make it impossible to detect without blocking the probe itself. In our case, the sample is titled downwards by a small angle of $\sim 5°$. In the scheme of the setup principle (Figure 2.2) it is drawn at a slightly bigger angle just for illustrative purposes. The scattered beam is focalized in the detector by a plano convex lens ($f = 10$ cm) and recorded by a lock-in amplifier.

For the transmission configuration, it is instead advisable that the sample surface is orthogonally placed respect to the scattering plane, so that not only the overlap of the pumps is optimized but also the superposition of the grating region with the probe beam is maximized. The scattered beam is collimated by L4 ($f = 20$ cm) and focalized in a 2151 Newport femtowatt photoreceiver by L5 ($f = 10$ cm). This photoreceiver is an extremely sensitive detector to be used in synchronous detection with a lock-in amplifier.

The lock-in amplifier used is a SR850 by Stanford Research Systems. The signal is acquired directly using an homemade LabVIEW software. The experimental need and advantages of using a lock-in amplifier when dealing with very small signals will be discussed in Section 2.4.

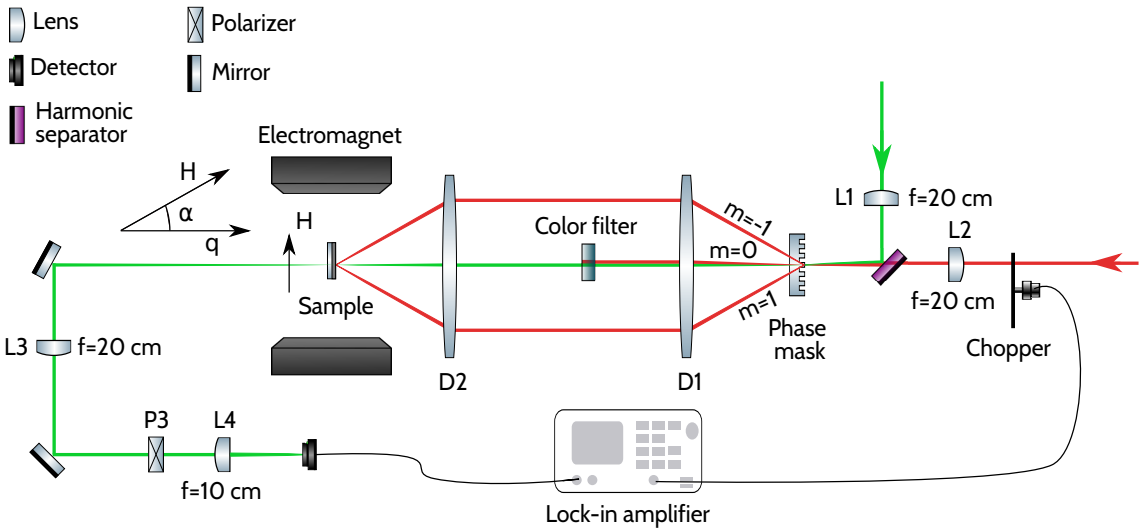

Figura 2.4: Faraday probe setup. The two first orders of the 1030 nm interfere on the sample generating the TG. The probe consists in the zero order of the 515 nm beam and a filter is needed to separate the two colors. The polarizers P3 is set to reach complete extinction. The electromagnet generates an in plane magnetic field at small angle α respect to the wave vector $\vec{q}$ of the acoustic waves excited by the TG.

2.3 Faraday probe setup

Our research goal is to probe the coupling of the surface acoustic waves generated in the substrate by the TG and the average out of plane magnetization component. In order to pursue this result we have combined the TG pump-probe with a magneto-optical analysis of the response to the probe. We integrate our setup with a Faraday spectroscopy configuration, allowing to measure the polarization changes of the transmitted probe beam, i.e after crossing the ferromagnetic Ni thin film. The measurement of the out of plane magnetization change M_z is straightforwardly given by the Faraday rotation.

The Faraday probe setup is the same as the pulsed TG in transmission, except for the final stage sketched in Figure 2.4. While the pump beams are obtained in the very same way as for the TG setup, the probe consists in the zero diffraction order of the 515 nm beam. As the zero orders of the pump and probe coincide, a color filter is used to get rid of the 1030 nm. This is necessary to avoid additional heat load on sample that could induce some unwanted dynamics.

To study the magnetoelastic coupling, an electromagnet is needed for two main reasons: to set the saturation magnetization of the sample in the wanted direction and to study the dependence of M_z on the applied magnetic field, which should show the expected resonances of the FMR with the SAWs generated by the TG. Figure 2.5 shows a picture of the sample placed in the air gap. The electromagnet is placed so that it generates an in plane external magnetic field, at a small angle α respect to the TG $\vec{q}$ vector on sample. At the present time, it is neither possible to measure α with precision nor to change it systematically. All the measurements presented in this thesis were made with an $\alpha \sim 5°$.

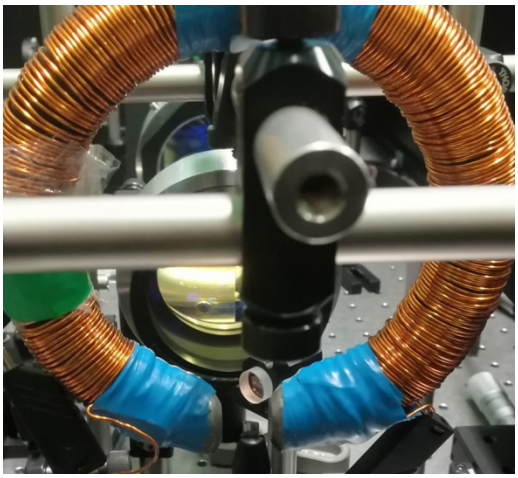

Figura 2.5: Picture of the sample in the magnet air gap.

In order to detect time resolved changes in the diffracted probe polarization, the polarizer P3 is set to reach total extinction. The lens L3 that collimates the diffracted beam is necessary to be sure that the polarizer works at its best. The detector is same femtowatt photoreceiver used in the pulsed TG setup. As the SAWs that induce the magnetization dynamics are generated by the TG, also in this case placing the sample in the focus is extremely crucial to observe a good Faraday signal.

2.4 Why a lock-in amplifier?

A lock-in amplifier is a very powerful instrument when measuring signals in a very noisy environment, also in case of noise up to a million times higher than the signal of interest [56]. Let's consider an experimental situation where we want to measure a very weak signal. Every optical signal is converted in an electronic one by the photodiode, which implies the presence of an electronic noise background that should be discriminated from the wanted signal. Therefore, the output signal can be express [57] as

$$V_s(t) = V_0(t) + V_{WN}(t) + V_{1/f}(t) \tag{2.2}$$

where $V_0(t)$ is the response of the system under analysis, V_{WN} is the white noise and $V_{1/f}$ is the so-called "1/f" noise. The noise spectrum of a typical experiment is shown in Figure 2.6. The white noise term can be expressed as $V_{WN} = V_{offset} + V_{wn}(t)$, where V_{offset} is a constant level and $V_{wn}(t)$ represents the random fluctuations. Therefore, it is possible to reduce $V_{wn}(t)$ simply by integrating over time. Despite this, even if we imagine to average for a very long time and ideally we menage to get rid of V_{offset}, at low frequencies the signal would be still dominated by $V_{1/f}$. This is a low-frequency noise with power spectrum inversely proportional to the frequency that can be traced back to electronic devices.

A powerful method to improve the signal to-noise-ratio is to modulate the signal at high frequency by using a chopper, in our case a mechanical one (MC2000B-EC from Thorlabs). First of all, this allows to eliminate the V_{offset} contribution by

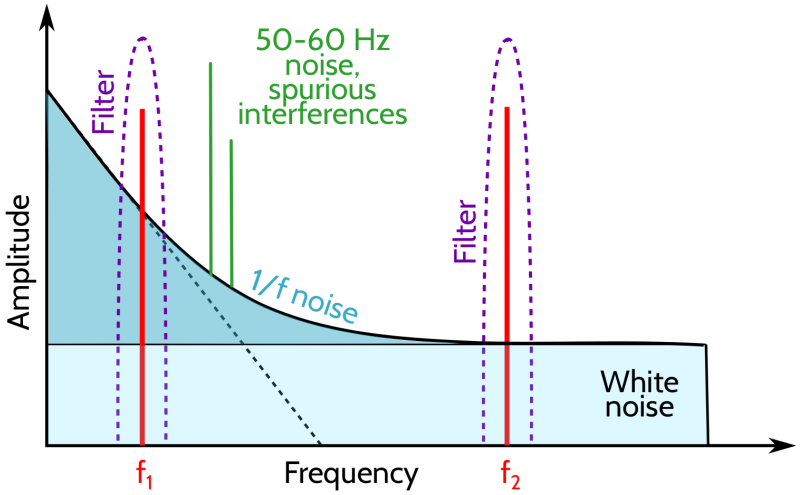

Figura 2.6: Typical qualitative noise spectrum in an experiment. Lock-in amplifiers allows to shift the measurements in regions with small background signal, avoiding the 1/f noise and interference of spurious frequencies coming from technical sources. It can be seen why picking the right signal modulation frequency can significantly affect the signal-to-noise ratio. Indeed, keeping the same filter bandwidth, at low frequencies such as f_1, the overall noise is much higher with respect to the high frequency region; therefore, choosing a high enough chopper frequency, like f_2, will yield a cleaner signal. Adapted from [56].

making the difference between the measured voltage when the signal passes through the chopper blades and when it does not. Secondly, by choosing an high enough chopper frequency and using it as external reference in a lock-in amplifier, it is possible to filter out the 1/f noise shifting the measurement at higher frequencies. However, the chopper frequency has to be much lower than the laser repetition rate. This is quite an important point because it means that many pulses can pass through the spatial window scanned by the chopper blades, so that one has enough statistics to choose a longer integration constant and hopefully increase the signal-to-noise ratio removing the V_{WN} time dependent component.

The basic operating principle consists in a homodyne detection scheme and a low pass filter that allow to measure the signal's amplitude and phase relatively to a given periodic reference signal. This allow to extracts the signal in a bandwidth centered around the reference frequency, efficiently cutting off all the others frequency components.

The lock-in takes in the signal $V_s(t)$ of interest along with the noise as well as the reference signal $V_r(t)$ and puts them through a frequency mixer, which is equivalent to a multiplication of the two input signals and best understood in the frequency domain. When the signal and the reference are two sine waves, the multiplication of this two signals gives

$$V_s(t) \cdot V_r(t) = A_s A_r \sin(\omega_s t + \theta_s) \sin(\omega_r t + \theta_r) = \\ \frac{1}{2} A_s A_r \Big(\cos((\omega_r - \omega_s)t + \theta_s - \theta_s) - \cos((\omega_r + \omega_s)t + \theta_s + \theta_s) \Big), \quad (2.3)$$

where A_s, ω_s and θ_s are respectively amplitude, frequency and phase of the signal and A_r, ω_r and θ_r are the analogous quantities of the reference. It can be seen from

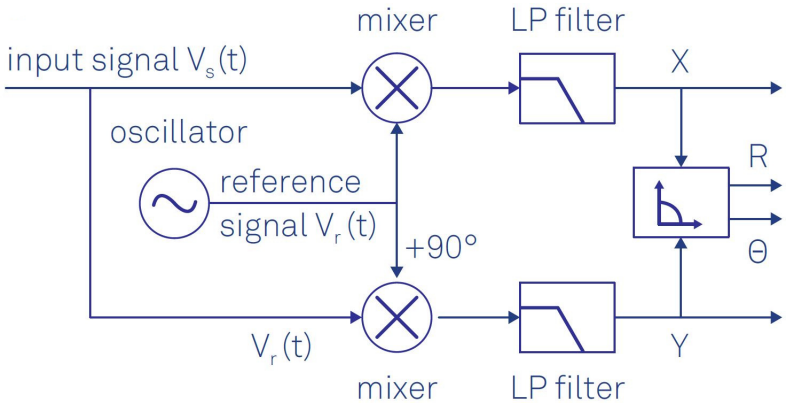

Figura 2.7: Dual-phase demodulation circuit scheme. Image from[56]

2.3 the multiplication simply gives two components with the sum and the differences of the two frequencies. Since the chopper frequency is also the external reference of the lock-in, we end up with DC component and the other at twice the chopper frequency. After mixing the DC component is isolated applying an adjustable low pass filter. The entire principle of mixing frequency and subsequent low pass filtering is called phase sensitive detection or demodulation.

The filter main features are bandwidth and filter order. The bandwidth is the frequency where the signal power is reduced by half; this frequency is inversely proportional to the chosen time constant, which is the lock in integration period. In choosing the bandwidth a mediation has to be done. Indeed, not only a wide bandwidth means more noise in the output signal but also it will lead to systematic measuring errors because some of the non-DC component may leak into the output signal. On the other hand, a narrow bandwidth will lead to lower time resolution and long measurements. The shape of the filter can be adjusted also by choosing its order, which indicates how many identical filter are cascated. A higher order leads to more ideal rectangular filter transfer function that cut off frequencies outside the frequency bandwidth more efficiently but takes more time to settle, which can cause a phase delay. On the contrary a lower order filter has the advantage to cause a lower phase and temporal delay, but it is less efficient in cutting off frequency.

As we have a non sinusoidal signal, demodulation can be understood using the Fourier theorem. It states that every periodic signal can be express as

$$V_s(t) = \sum_n \; x_n \cos\left(n \; f_r + \theta_n\right) \; + i \; y_n \sin\left(n \; f_r + \theta_n\right), \tag{2.4}$$

where f_r is the reference frequency, x_n and y_n are the two amplitudes corresponding to the n-th harmonic of f_r and θ_n is a phase factor.

Demodulation applied to such an expression means selecting the components with frequencies within one filter bandwidth around the reference frequency. In the case of an ideally narrow bandwidth, the lock-in reduces the infinite sum to a single cosine and sine terms. Actually, in order to measure amplitude $R(t)$ and phase $\theta(t)$ of the signal $V_s(t)$ the so-called dual-phase demodulation circuit is usually used. As can be seen in Figure 2.7, the signal is split to obtain the two Fourier components.

The $X(t)$ in-phase component corresponds to cosine wave demodulation, while the other independent Fourier component, usually called $Y(t)$ or quadrature component, is obtained performing the demodulation with a sine wave, which corresponds to delaying the reference by 90°. The amplitude $R(t)$ and the phase $\theta(t)$ of the signal of interest are then easily derived from $X(t)$ and $Y(t)$ by a transformation from Cartesian coordinates into polar coordinates using the relations

$$R(t) = \sqrt{X(t)^2 + Y(t)^2},$$

$$\theta(t) = \text{atan2}(Y(t), X(t)),$$

where the atan2 is used instead of atan to obtain a phase in the range $[-\pi, \pi)$.

To achieve high signal-to-noise ratio it is also necessary to adjust some other lock-in parameters, such as the input range and sensitivity. Furthermore, DC component of the input signal can use up the most of the lock-in dynamic reserve, resulting in reduce measurement performance. Setting the input to AC coupling adds a high pass filter on the input signal that removes this DC offset. For this reason, all measurements were taken with the AC input coupling.

Choice of the lock-in parameters

As mentioned in the previous section, the lock-in parameters need to be properly set according to the signal of interest in order to achieve high signal to-noise-ratio. We found that a time constant of 300 ms with a low pass filter of 18 dB is the optimal experimental condition, which we kept for all the measurements presented in this thesis. Input range and sensitivity need to be adjusted each time depending on the signal in order to avoid respectively input and output saturation. However, the key parameter to obtain the optimal signal-to-noise ratio is the chopper frequency, which is used as external lock-in reference frequency. We identified 719 Hz as a good working condition for two main reasons. Firstly, because 719 is a prime number and it is quite unlikely to find spurious interference frequencies and/or their harmonics. Secondly, 719 Hz it is high enough to obtain a good signal-to-noise ratio but still below 735 Hz, which is our detector frequency bandwidth.

2.5 Phase mask and doublets: advantages and features

As other ultrafast optical techniques, TG spectroscopy involves the crossing at non-zero angle of femtosecond pulses on the sample. It was proved in 1998 [58] that an efficient way to recombine such short pulses is to use a configuration in which, upon diffraction of a short pulse by a phase mask, the first-order diffraction maxima are recombined at the image plane by a system of two identical confocal doublets. We implemented such configuration, as shown in the setup schemes (Figure 2.2 and 2.4).

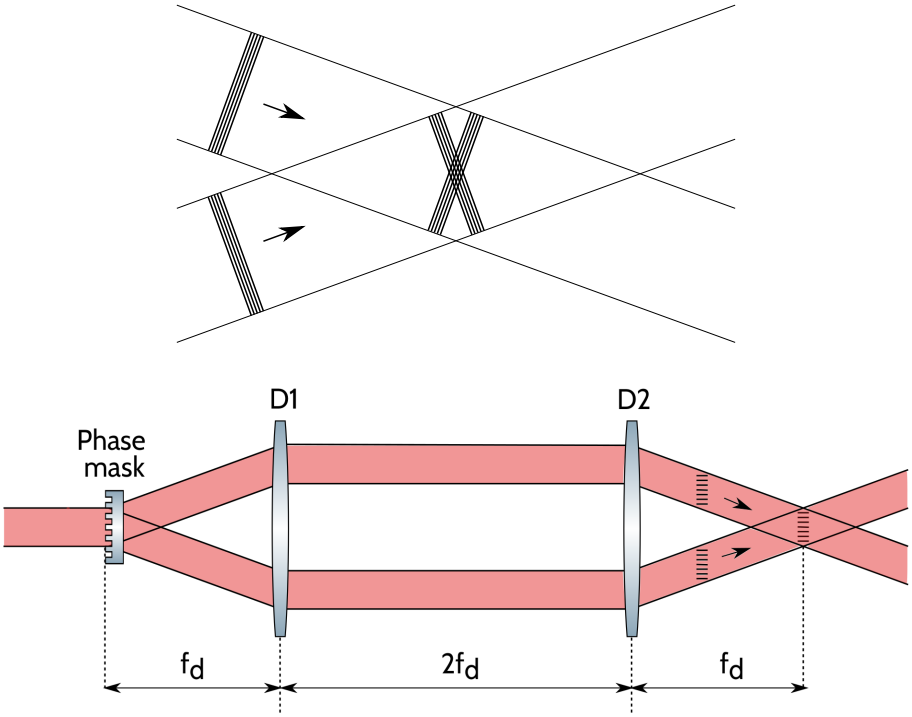

Figura 2.8: Crossing of short pulses. The overlap area of two short pulses can be very small without phase mask (top panel). When using a phase mask combined with two doublets in confocal configuration (bottom panel), the overlap area increases because of the parallel pulse wavefronts of the diffraction orders. The confocal characterization consists in placing the doublets at twice their focal length $f_d = 10$ cm. Adapted from [58]

It is known that the shorter the pulses, the smaller the overlap area, as can be seen in the top panel of Figure 2.8. In particular, for two beams crossed at an angle θ_{ex}, the size of the overlap area is given by [58]

$$A = \frac{c\tau}{\sin(\theta_{ex}/2)}, \tag{2.5}$$

where c is the speed of light in the medium and τ is the pulse duration. Furthermore, the number of interference fringes produced by two beams is independent of the angle and roughly

$$n_f = \frac{2c\tau}{\lambda_{ex}} \tag{2.6}$$

Depending on the specific experimental parameters, A can become very small and greatly reduce the efficiency of the TG. Furthermore, the shorter the pulses become, the harder is to simultaneously achieve spatial and temporal overlap, which is a crucial condition to observe the TG signal.

These limitations can be overcome when crossing diffraction orders of a phase mask using two identical doublets in confocal configuration, as depicted in the bottom panel of Figure 2.8.

Basically, doublets are a diverging and converging lenses with different refractive index paired together. Usually, in the making process much attention is given to

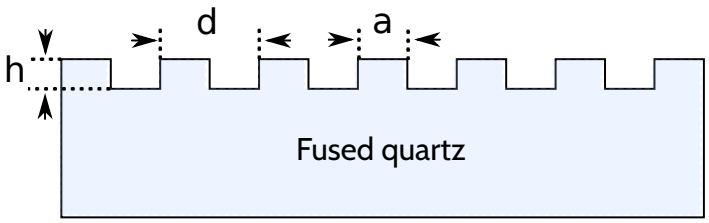

Figura 2.9: Phase mask scheme.

constructive details such as dimension, shape and curvature, in order to reduce as much as possible spherical, chromatic and spatial aberrations. The doublets used in our setup are made with some specific features by Tecnoottica Consonni. First of all, they are achromatic, as they need to work equally well for the 1030 and 515 nm. They are also specifically designed to have a big diameter and be able to work well even when the incident beams are close to the edge. Indeed, this guarantees that the doublets are suitable for different masks and that the two colors are focalized in the same point in the image plane of D2.

Let's see why the use of the phase mask combined with this imaging system is particularly convenient in overlapping two pump pulses. The main reason is that each diffraction order have tilted pulse fronts, but the pulse fronts of the two different diffraction order turn out to be parallel. This greatly expand the overlap area, which in this case turns out to be equal to $c\tau$. The confocal configuration consists in placing the doublet D2 at twice their focal length ($f_d = 10$ cm). It can be shown that this arrangement not only provides pulse overlap in the image plane but also preserves short pulse duration [58]. Furthermore, the TG generated on sample has a well defined and easily tunable periodicity given by the phase mask features. Indeed, this imaging system creates in the image plane of D2 an image of the phase mask grating with periodicity $\Lambda = d/2$, where d is the periodicity of the phase mask grating. Therefore, the confocal configuration combined with a phase mask allows to generate an efficient TG with a well known periodicity in a relatively simple way.

As mentioned earlier, the two pump pulses given by the diffraction orders are recombined in the focal plane of D2, generating the TG by interference. The TG has therefore the same temporal length of the pump pulses; its spatially extension can be easily calculates as $c\tau$. As the two pump pulses begin to overlap, the grating starts to generate. Propagating further, the overlap region becomes bigger, until complete superposition is achieved. In this situation, which is depicts in Figure 2.8, the maximum efficiency is reached. As the pulses continue to propagate, the grating becomes less and less efficient, until it disappears.

Some important features of the phase mask are the material, the thickness, the depth and periodicity of the engravings. In Figure 2.9 a schematic sketch of the phase mask is shown. Choosing the right material and thickness can be critical to preserve the quality of the diffraction orders and to improve the focal spot stability, as it will be explained in Section 2.6. Our phase masks are created by lithography on 1 mm thick Ted Pella fused quartz slides.

As mentioned earlier, the phase mask periodicity d defines the periodicity of the TG. It is well known from geometrical optics that

$$d = \frac{m\lambda}{\sin(\theta_m)} \tag{2.7}$$

where λ is the wavelength of the incident beam and θ_m is the diffraction angle of the m-th diffraction order. It can be easily derived from equation 2.7 that, as the probe is obtained from SHG ($\lambda_{pump} = 2\lambda_{probe} = 1030$ nm), the first diffraction orders of the pump coincides with the second diffraction orders of the probe. Anyway, they are negligible compared to the pump intensities.

Combining Equation 1.2 and 2.7 it is clear why, when performing measurements varying the q on sample, the use of phase masks with different d are experimentally convenient rather than realigning each time the pump beams at different incidence angles. From considerations about the sound velocity in our sample, we calculated $d \leq 8$ µm to guarantee an appropriate number of oscillations in the TG signal.

Regarding the grooves depth h, it plays an important role in the diffraction order efficiency. To derive it, we can consider an incident beam as a plane wave with wavelength λ under normal incidence. The phase ϕ of the light that passes through the grating is modulated according to the phase mask profile. The phase shift can be expressed as [59]

$$\Delta\phi = \frac{2\pi h \Delta n}{\lambda} \tag{2.8}$$

where Δn is the refraction index mismatch at the air/fused quartz interface. In case of gaussian beam and a rectangular phase mask with a grating duty cycle parameter $D = a/d$, the efficiency η for the zero order is

$$\eta_0 = \cos^2(\Delta\phi/2) \tag{2.9}$$

while for the m-th diffraction order ($m \geq 1$) can be expressed as

$$\eta_m = \frac{4}{\pi^2 m^2} \sin^2(\pi m D) \sin^2(\Delta\phi/2) \tag{2.10}$$

In Figure 2.10 are displayed the efficiencies calculated considering a phase mask made of fused quartz ($n^{1030} = 1.4500$, $n^{515} = 1.4615$) with $D = 0.5$ and combining equations 2.9 and 2.10 with 2.8. As in the experiment the first diffraction orders are used, we chose h to maximize the efficiency of pump and probe first diffraction orders rather than the zero order. We identified $h \sim 750$ nm as a good nominal grooving depth.

Phase mask fabrication and characterization

The phase masks were made in the CNR-IOM TASC laboratory using UV lithography. Detailed information regarding the fabrication method can be find at reference [60].

As shown in Figure 2.11, the phase mask is placed on a rotating mount to obtain the scattering plane parallel to the optical axis. In order to check the quality of

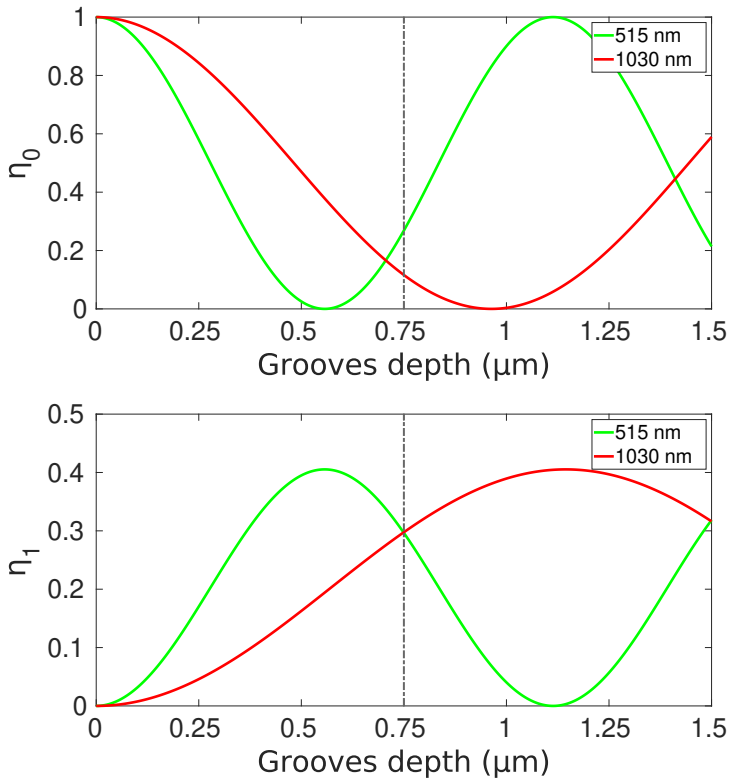

Figura 2.10: Efficiency of the zero (top panel) and first diffraction orders (bottom panel) for $\lambda_{pump} = 1030$ nm and $\lambda_{probe} = 515$ nm. The gray dashed lines is placed at 0.75 µm, the nominal depth we identified as optimal.

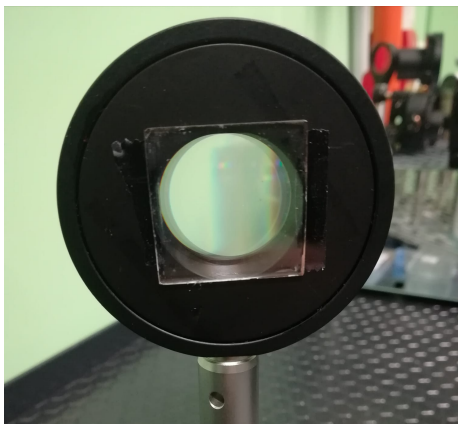

Figura 2.11: Phase mask on the rotating mount.

this fabrication procedure, an AFM measurement was performed on the phase mask having $d = 5$ µm.

AFM scans have been performed in ambient conditions with a Solver Pro (MT-MDT) instrument, in semicontact mode using commercial cantilevers (NT-MDT, NSG30, nominal spring constant $k = 40$ N m^{-1}, nominal radius of curvature < 10 nm). A 20 µm x 20 µm area was scanned with samplings of 256 pixels in both directions. To obtain the data displayed in Figure 2.12, the raw data were leveled by a mean plane subtraction and a row alignment. From this measurements we extracted $d = 5$ µm and $h = 724$ nm.

d and h can also be estimated optically. Actually, the periodicity of the phase mask and the q on sample can be estimated quite accurately respectively from equations 2.7 and 1.2. In order to measure θ_m we placed the phase mask at a known distance from a reference sheet. The angle θ_m can be easily obtained by measuring the distance between the spot of the m-th order and that of the zero order.

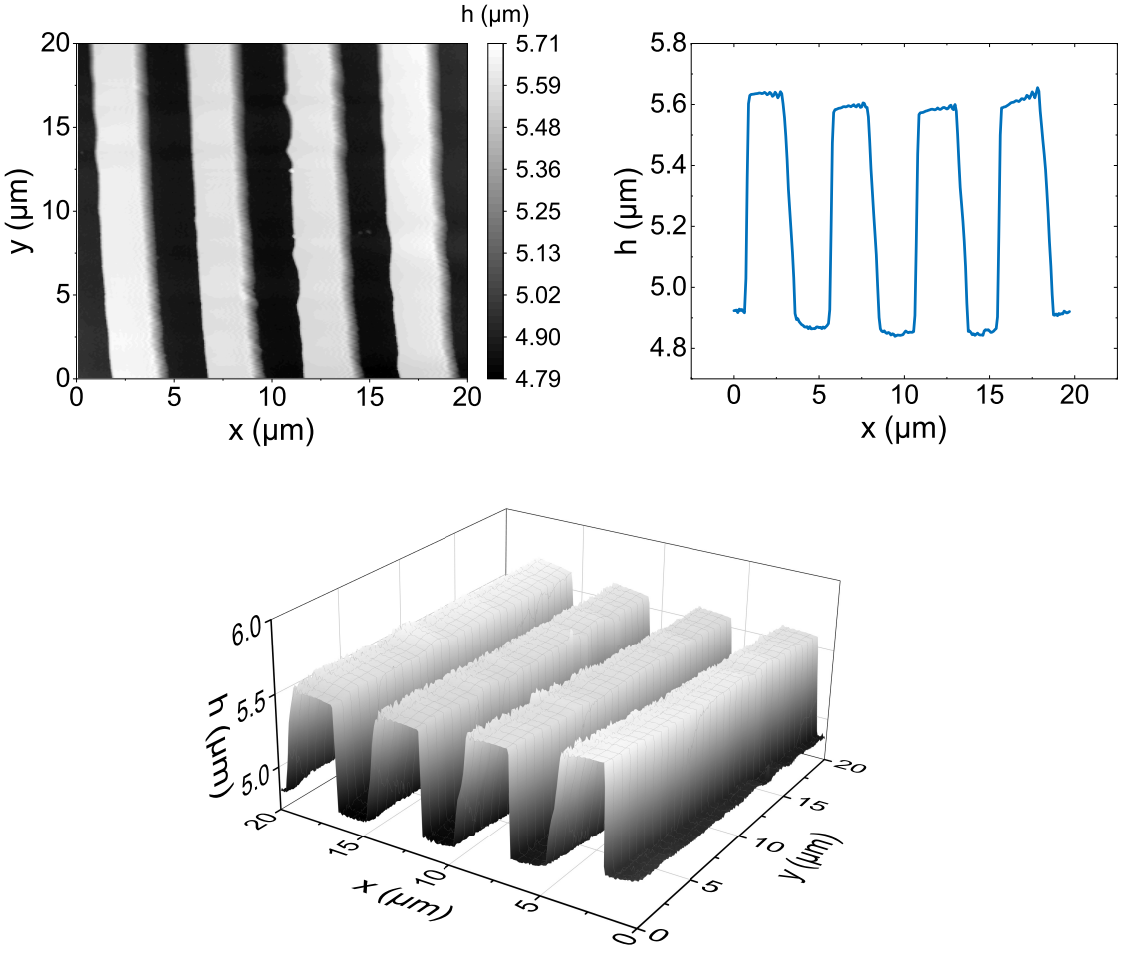

Figura 2.12: AFM measurement of the $d = 5$ µm phase mask. The scanned area is 20 µm x 20 µm. The data are presented as a 2D surface map (top left panel), a graph of the phase mask profile (top right panel) and as a 3D surface (bottom panel).

λ (nm)	m	θ_m (°)	d (µm)	q (µm^{-1})
1030	+1	11.6	5.09	2.47
515	+1	5.9	4.99	2.51

Tabella 2.1: Estimates of θ_m, d and q calculated from both the pump and probe first diffraction orders of the $d = 5$ µm phase mask. The results for $m = -1$ is not reported because the results are identical to those for $m = 1$. The error on these three quantities has been calculated by error propagation starting from the measured distances and in each case is less than 1%. To obtain these small errors the phase mask was placed ~ 1.5 m away from the reference screen.

λ (nm)	m	P_m (mW)	η_m	h (µm)
1030	0	171	0.2	675
	+1	264	0.3	745
	−1	263	0.3	745
515	0	18	0.32	765
	+1	10.2	0.18	855
	−1	9.84	0.18	855

Tabella 2.2: Estimates values of h from $d = 5$ µm phase mask diffraction efficiencies. P_{in} for the 1030 nm and 515 nm are respectively 0.87 W and 55.4 mW.

We did it for the first two diffraction orders of both the pump and probe, and the obtained estimates of θ_m, d and q for the $d = 5$ µm phase mask are shown in Table 2.1. The obtained values of d are essentially the same for the two wavelengths and in perfect agreement with what was measured with the AFM. Furthermore, the estimates of q using Equation 1.2 will be used later on in the calculation of sound velocity of the acoustic waves launched by the TG.

Regarding the grooves depth h, it can be estimated starting from the measured phase mask efficiencies

$$\eta_m = \frac{P_m}{P_{\text{in}}}, \tag{2.11}$$

where P_m and P_{in} are respectively the measured power of the the m-th orders and the incident beam, which can be easily measured using a power meter. Having η_m it is then possible to extrapolate h from the graphs in Figure 2.10. In Table 2.2 are shown the calculated values of h from the two different wavelengths and considering different diffraction orders. The differences between the measured and calculated values can be ascribed to the approximation used in Equations 2.9 and 2.10 which do not take into account the gaussian beam profile. Otherwise, the optical estimation can be considered quite good.

We therefore used the same approach to fabricate two other phase masks with $d = 6$ µm and $d = 8$ µm, which have been only optically characterized. Table 2.3 summarizes all the parameters obtained for each mask. The followed procedure is the exact same as for the $d = 5$ µm phase mask.

d (µm)	$\theta_{ex}/2$ (°)	θ_{probe} (°)	q (µm $^{-1}$)	h (µm)
5.09	11.6	5.9	2.47	~ 770
6.01	10	4.9	2.05	~ 830
8.00	7.5	3.7	1.57	~ 600

Tabella 2.3: Phase mask parameters extracted by optical characterization.

2.6 Focal spot characterization

In order to observe a good TG signal, not only the pumps must be temporally and spatially overlapped, but also the sample must be placed in the focal plane. These are key aspects to increase the efficiency of the TG signal, and the possibility to finely tune the sample position in the focal plane it is extremely useful. In order to have a precise control on the position of the sample, it was mounted on a "clamp" sample holder positioned on coupled translators that allow to move the sample both parallel and perpendicular to the optical axis with a precision ~ 10 µm. The movement perpendicular to the optical axis allows to shift horizontally on the sample surface and is particularly useful in the testing phase if it happens to damage locally the sample. Moving the sample in the direction of the optical axis instead allows a fine tuning of the position of the sample in the focal plane, in order to optimize the TG signal.

As in any pump-probe measurement, the probe beam has the only purpose to probe the dynamic induced by the TG and it is desirable that not only the probe beam spot in the focal plane is smaller than the pump one, but also that the probe fluence on sample is less than the pump one, to be sure that the probe does not induce any additional dynamics. In order to check the relative dimension of pump and probe spot in the focal plane, a beam profiler was placed in the sample holder position and some images were acquired scanning different positions around the focal plane. These CCD images are displayed in Figure 2.13. Before and after focal plane the pump and the probe spots are clearly distinguishable. As expected, in the focal plane the three beams nicely overlap and their photon density greatly increases. The elliptical shape of the spots is due to non-perfect alignment conditions during the measurement that cause the scattering plane not to be perfectly perpendicular to the surface of the CCD, causing a deformation of the beam spot. Although it is preferable that the scattering plane is perpendicular to the sample surface, this does not affect the efficiency of the four-wave mixing process. Even if the two images are taken symmetrically before and after the focal plane, they are not identical; this is expected when working with diffraction orders that undergoes scattering processes instead of ideal gaussian beams.

In order to measure the spot size of both pump and probe beams, similar images in the focal plane of only the pump and the probe were also taken. The spot size was calculated with the BeamGage software. The pump beam FWHM along the major axis is 55.2 µm while along the minor axis is 43.7 µm; similar measurements for the probe beam give respectively 40.7 µm and 31.0 µm.

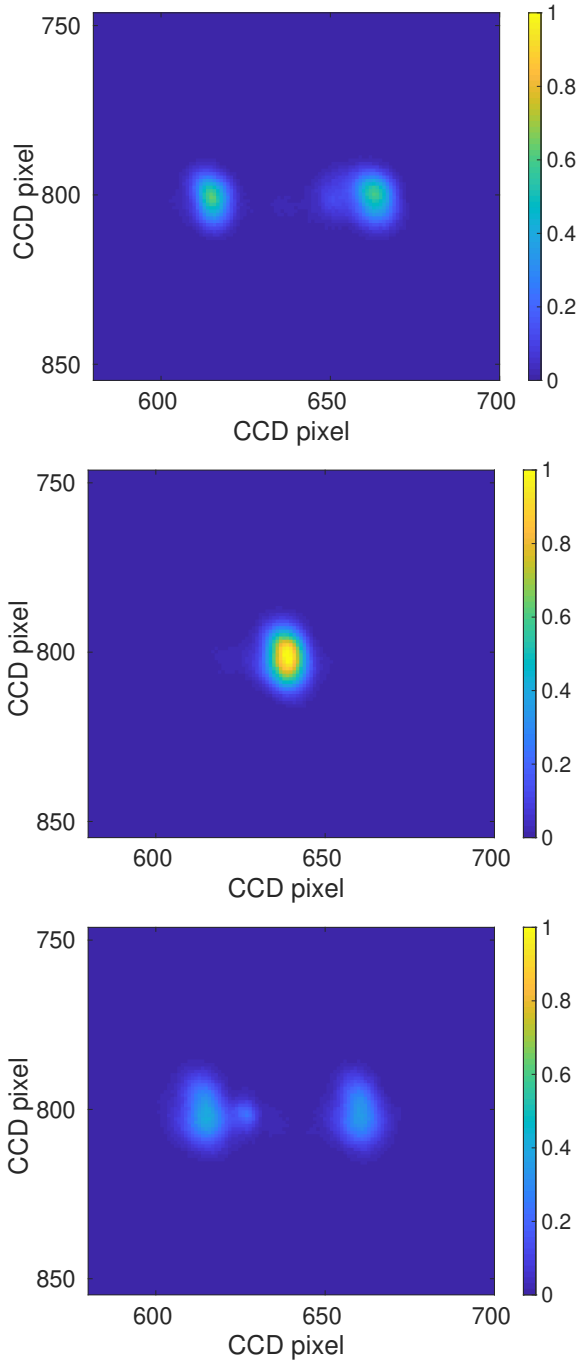

Figura 2.13: From top to bottom: images captured by the beam profiler CCD camera before, in the focal plane and after. As the CCD camera of the beam profiler is very sensitive, several neutral filters are needed to low the beam intensities. These images are taken with a pump and probe energy on the CCD respectively of 0.6 µJ/pulse and 0.2 nJ/pulse.

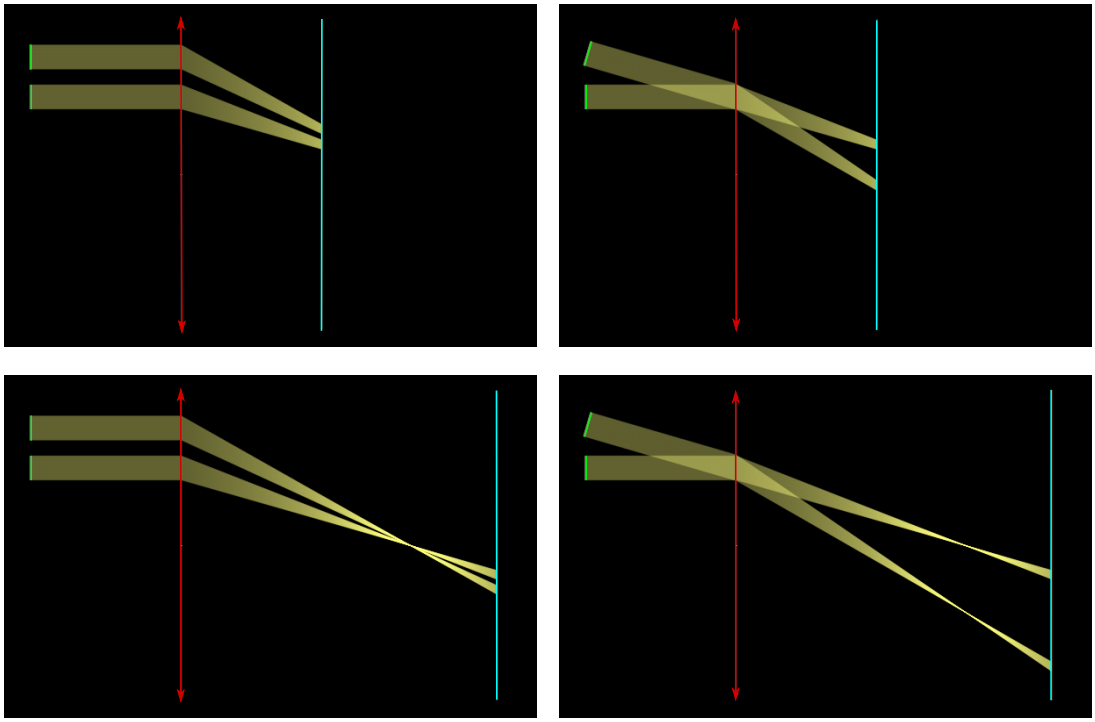

Figura 2.14: Optical simulation of a beam passing through an ideal lens (in red). In order to measure pulse fluctuation in the focal plane the beam profiler (in blue) has to be placed slightly out of the focal plane. When there are only fluctuations parallel to the propagation direction, placing it before (top left panel) or after (bottom left panel) gives approximately the same results. In case of fluctuations in the $\vec{k}$ direction, placing it before the focal plane (top right panel) could underestimate the focal plane displacements. For small $\vec{k}$ fluctuation, testing the stability before or after the focal plane is equally effective.

Considering that the signal depends on the spatial overlap of the three beams, and that the measurements could be really long (several hours), it is important to evaluate the fluctuations of the three beams at the sample position. The easiest way to investigate fluctuations of the absolute focal spot position is placing the beam profiler in the focal plane. However, this is not effective if we are interested also in quantifying the relative displacements because the beam profile would not be able to resolve the pump and probe beam spots, when completely overlapped. Nevertheless, it is possible to overestimate these displacements acquiring images of the beam spots slightly out of the focal plane. Figure 2.14 displays some basic optical simulations made to qualitatively understand where the beam profiler could be conveniently placed. These simulations show how the focus position of an ideal lens is affected by $\vec{k}$ fluctuations of the incident beam. This can be understood in the framework of the Fourier optics [38]. A beam with a given $\vec{k}$, when passing through an ideal lens, undergoes a variation of amplitude and phase and produces a spectrum of plane waves that turns out to be the its Fourier transform. Therefore, beams with different $\vec{k}$ are focused in different points of the focal plane, which is why lenses can be used as spatial filters to improve monochromaticity. It is then clear why the focus position in the focal plane is only affected by fluctuations in

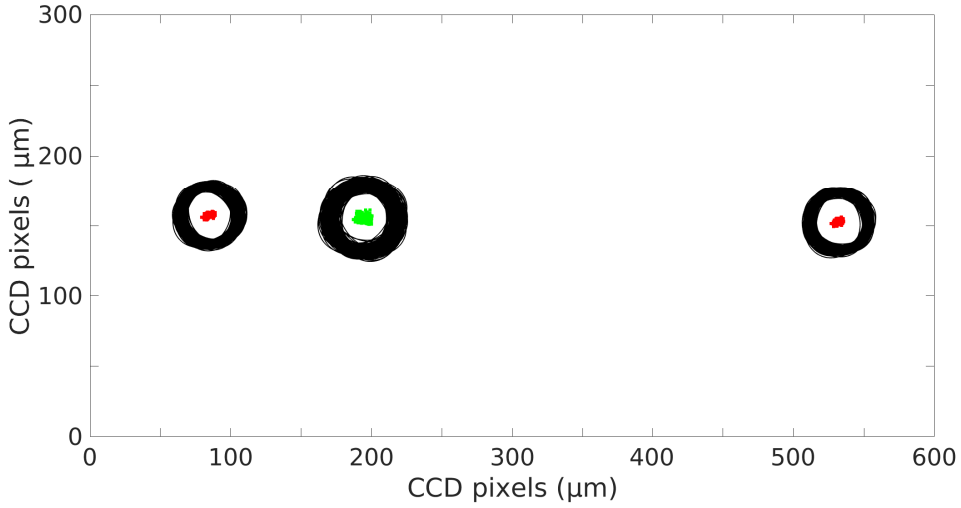

Figura 2.15: Stability measurement before the focal plane. The measurement was made at a repetition rate of 50 kHz and at pump and probe energy on the beam profiler CCD camera respectively of 0.15 nJ/pulse and 0.65 pJ/pulse. Spot position was acquired every 2 minutes for $\sim$ 12 hours. The spot centroids are marked with a dot, red for the pumps and green for the probe. The 2D FWHM of each acquired spot is reported with black ellipses. In all cases the fluctuations are inside the spot size.

the $\vec{k}$ direction. These kind of fluctuations are the most likely in our case, as they are mainly due to phase mask overheating. However, a general beam fluctuation can be seen as the combination of a fluctuation parallel to the propagation direction and a fluctuation of the $\vec{k}$ direction. As shown in Figure 2.14, placing the detector after the focal plane is the better way to take into account also the this kind of fluctuations. However, as the needed average power is very low (see Table 3.2), the expected fluctuations are very small and placing the beam profiler before or after the focus is equally effective.

In order to further overestimate the phase mask heating, the focal spot stability measurement was done at pump intensities much higher than the usual working condition (see Table 3.2). The pump and probe beam intensity were set respectively to 1.3 µJ/pulse and 1 nJ/pulse. The positions of the three beam spots before the focal plane were acquired every 2 minutes for $\sim$ 12 hours. Figure 2.15 displays the spot centroid and the 2D FWHM of each beam. The standard deviation of the centroid position turns out to be 1.5 µm for the pumps and 2.38 µm for the probe. The relative distances fluctuate 1 µm maximum. Since these are overestimates, they are negligible in the focal plane. Considering the dimension of the focal spot, the spatial stability can be considered greatly satisfying and fully adequate for the experiment.

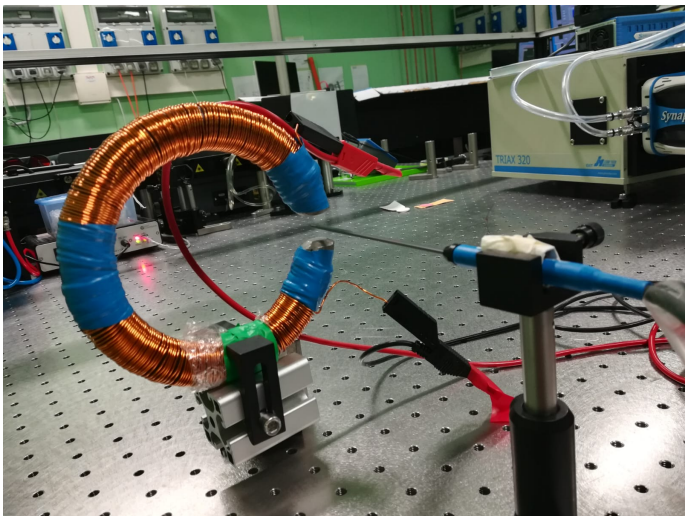

Figura 2.16: Measurement of the magnetic field in the air gap. The Hall probe was placed in the middle of the air gap to measure the magnetic field applied to the sample.

2.7 Magnetic field calibration

The external magnetic field needed to study the magneto-elastic coupling is provided by an homemade electromagnet. The magnitude of the external magnetic field H can be controlled by changing the current in the electromagnet windings. In order to check the quality of the magnetic field in the air gap and to be sure to properly control the external magnetic field applied to the sample, some tests were made. Firstly, the magnetic field in the air gap was measured using a gaussimeter (LakeShore 475 DSP). The Hall probe (Lakeshore HMMT-6J04-VR) was placed in the middle of the air gap, as shown in Figure 2.16. The measured magnetic field as a function of the applied current is shown in Figure 2.17. The observed hysteresis can be traced back to the magnetization hysteresis of the magnetic core, which is made of soft iron. As we expected to need in the gap air a magnetic field ≤ 500 G, the calibration was made varying the current in the $[-3, 3]$ A range. Because of this hysteretic behavior and in order to preserve repeatability, it is important to find a systematic way to control the magnetic field in the air gap.

In Figure 2.18 are shown some measurements made by varying the current in the electromagnet windings in different ranges. The main result is that a systematic way to obtain the values of Figure 2.17 is setting the current at 3A and varying it in the $[-3, 3]$ A range following the loop $3\text{A} \rightarrow 0\text{A} \rightarrow -3\text{A} \rightarrow 0\text{A} \rightarrow 3\text{A}$. This procedure is followed every time the electromagnet power supply is switched off and when the current is set at some other value outside the $[-3, 3]$ A range.

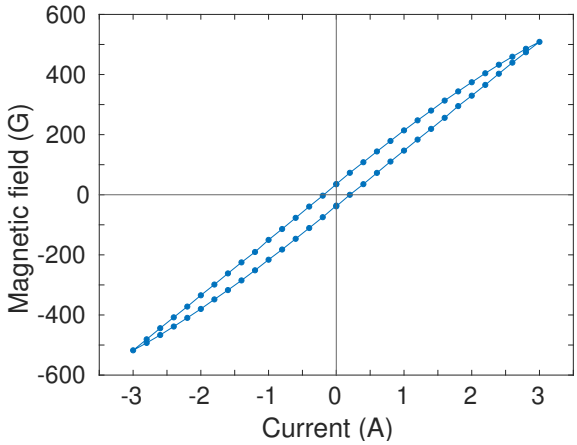

Figura 2.17: Calibration of the magnetic field in the electromagnet air gap. The applied current was varied considering the magnetic field interval of interest, because the hysteresis width changes depending on the maximum applied current. As we expected an external field on sample of 500 G to be enough for our purposes, we varied the applied current 3A $\rightarrow$ 0A $\rightarrow$ $-$3A $\rightarrow$ 0A $\rightarrow$ 3A with a 0.2 A step.

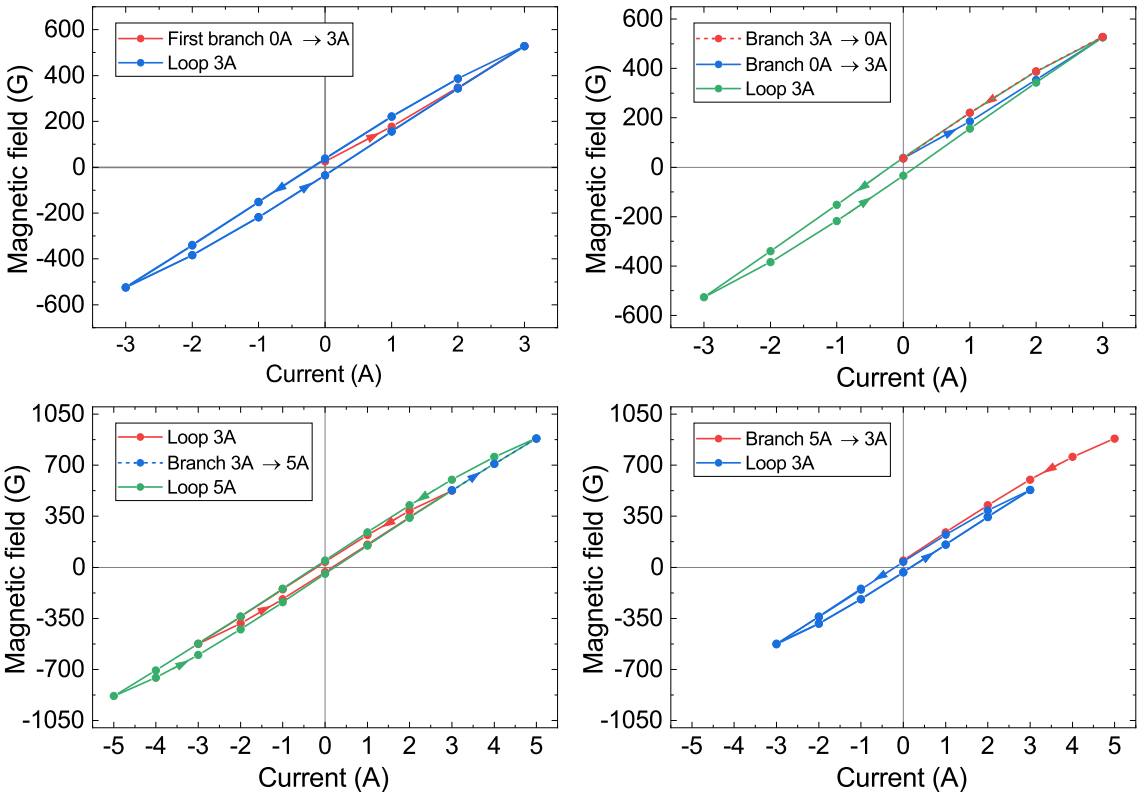

Figura 2.18: Magnetic field in the electromagnet air gap as a function of the applied current. Top left panel: when switching the power supply on and increasing the current 0A $\rightarrow$ 3A the magnetic field follows a path different from the loop obtained varying the current 3A $\rightarrow$ 0A $\rightarrow$ $-$3A $\rightarrow$ 0A $\rightarrow$ 3A . Top right panel: decreasing the current 3A $\rightarrow$ 0A, the path is the same as the 3A loop, but when the current is increased 0A $\rightarrow$ 3A it follows the same path as the first branch. However, the loop obtained changing the current 3A $\rightarrow$ 0A $\rightarrow$ $-$3A $\rightarrow$ 0A $\rightarrow$ 3A is repeatable. Bottom left panel: after doing a 3A loop, the current is increased 3A $\rightarrow$ 5A and a 5A loop is made. Bottom right panel: decreasing the current 5A $\rightarrow$ 0A it is always possible to return on the initial 3A loop.

The quality of the magnetic field in the air gap was also checked keeping the current constant at 3 A and changing the position of the Hall probe inside the air gap. With reference at Figure 2.19, the Hall probe was mounted on two coupled micrometric translators so that it could be finely moved along the x and y axis. The z positions were taken in the middle of the air gap and close to the poles. The magnetic field in the electromagnet air gap can be considered uniform for our purposes. In every measurement with an external magnetic field, the sample was placed in the middle of the air gap.

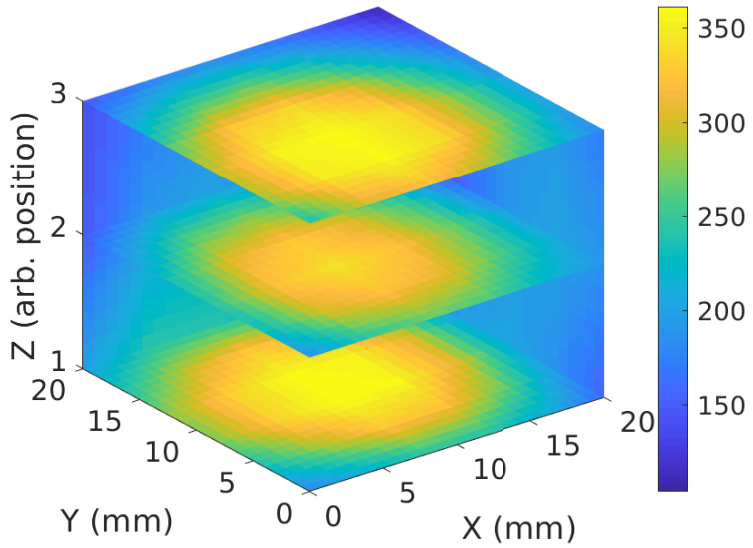

Figura 2.19: Scan of the magnetic field intensity in the air gap. The intensity is reported in G.

Capitolo 3

Experimental results and discussion

3.1 The sample: growth and magnetic characterization

The sample is a $\simeq 40 \pm 3$ nm thick polycrystalline Ni film deposited on 1 mm double polished Ted Pella fused quartz substrate, and protected by a 10 ± 2 nm thick SiO_2 capping. It was fabricated in the CNR-IOM TASC laboratory clean room facility. A schematic illustration of the sample is shown in Figure 3.1. The capping is necessary to preserve the Ni surface from oxidation, since the measurements are performed in air. Furthermore, it has to be transparent, in order to minimize its absorption and reflectivity to reduce the average power on sample. Indeed, if the capping absorbs and/or reflects the majority of the pumps power higher fluences are needed to excite and probe the acoustic (and spin) waves in the sample, with the consequence risk of damage.

Before the Ni deposition, the substrate was cleaned with acetone and then with ethanol to remove any residual acetone on the surface. The Ni thin film was grown using the electron-beam vapor deposition. With no chemical or physical treatments performed on the surface, the substrate was directly inserted in the vacuum chamber. A schematic illustration of the deposition chamber is shown in Figure 3.2. Electron-beam vapor deposition exploits a magnet to focus electrons from a heated filament and form an electron beam, which is directed toward a suitable crucible containing the material of interest. The electron energy is used to heat up the material, causing evaporation. The material vapors then travel out of the crucible and coat the substrate. In our case, an Alfa Aesar 99.995% pure Ni rod was placed inside

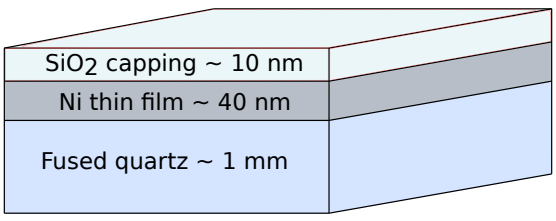

Figura 3.1: Schematic illustration of the sample.

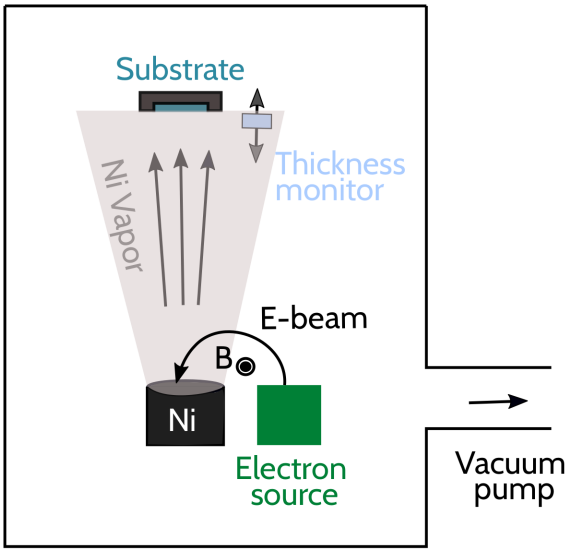

Figura 3.2: Scheme of the electron beam deposition chamber. An $\sim$ 10 keV electron beam is directed by a magnetic field toward a crucible containing Ni by an applied magnetic field. The electrons heat up the Ni inside the sample, causing evaporation. These atoms then precipitate into solid form, coating the substrate with a thin layer of the anode material. The thickness monitor consists in an off-axis α quartz substrate on a micro-oscillator.

a Tungsten crucible and heated up by a $\simeq$ 10 keV electron beam. The SiO_2 capping was grown with the same technique, starting from the Alfa Aesar 99.995% pure fused silica powder. The deposition parameters are shown in Table 3.1. In particular, the deposition rate depends on the position and orientation of the substrate in the chamber. Lower deposition rates correspond to better film quality and smaller errors on the film thickness. Deposition rates were measured using an $\alpha-$quartz piezoelectric micro-oscillator, which mechanically oscillates when an AC voltage is applied. The resonance frequency of the oscillations is dependent on the mass of the film deposited onto it. The Z-ratio is a parameter that corrects the frequency-change-to-thickness transfer function for the effects of acoustic-impedance mismatch between the crystal and the deposited material, allowing to derive the film thickness. Z-ratios are tabulated and easy to be found. More information about the electron-beam deposition facility at TASC laboratory can be found in Reference [61].

	P (torr)	T (K)	E.R. (Å/ s)
Ni	$9 \cdot 10^{-7}$	300	0.1
SiO_2	$1.3 \cdot 10^{-6}$	300	0.3

Tabella 3.1: Electron gun vapor deposition pressure (P), temperature (T) and evaporation rate (E.R.) of Ni and SiO_2. In both cases the deposition took place at room temperature (300 K).

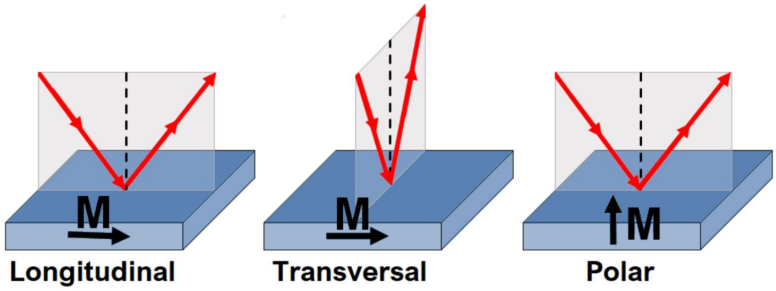

Figura 3.3: The three possible MOKE geometric configurations. The red arrows indicate the light propagation direction $\vec{k}$, while the magnetization $\vec{M}$ is represented in black. Image from [62].

In order to magnetically characterize the sample, Magneto Optical Kerr Effect (MOKE) measurements were performed at the NFFA facility in connection with the APE-HE beamline of IOM at Elettra. In the visible the Kerr effect is determined by the same matrix elements derived in Section 1.4 for the Faraday effect, however it is measured in reflection geometry. The Kerr effect can be easily measured with two crossed polarizer and a lock-in amplifier, in the same way as the Faraday effect.

Once the scattering plane is set, the polarization of the incident light can be decomposed into a parallel and a perpendicular component. The variations of these two components in the reflected beam with respect to the incident one provide information about the magnetization of the sample. Depending on the magnetization direction with respect to the sample surface and the incident light wave vector, three MOKE geometric configurations can be distinguished: polar, longitudinal and transverse. These three configurations are schematically represented in Figure 3.3 and each of them is predominantly sensitive to a different component of the magnetization vector. Longitudinal and transverse Kerr effects are sensitive to the in-plane magnetization components, respectively parallel and transverse to the light incidence plane. The polar Kerr configuration probes instead the out-of-plane component. The setup used for our measurements is based on the longitudinal MOKE geometry. The sample can be rotated around the axes normal to the sample surface, probing the variation of the magnetic response as a function of the angle between the applied field $\vec{H}$ and the initial in plane direction. In our case it was arbitrarily taken parallel to one of the sample edges. The in-plane magnetic anisotropy was probed by acquiring hysteresis loop at different angles. The laser source used is a 658 nm continuous low power WorldStarTech TECBL-10GC laser diode. A detailed description of this experimental MOKE experimental setup can be found elsewhere [62, 63].

Figure 3.4 shows the hysteresis loops of the sample rotated by different angles. As expected for a magnetic thin film, the hysteresis loops are squared and presents a remanence close to the magnetization at saturation, meaning an in-plane easy magnetic anisotropy. However, since the in-plane rotation of the sample does not affect significantly the hysteresis loop, the in-plane anisotropy has no magnetic preferential direction. Furthermore, the measured coercive and saturation fields are respectively $H_c \simeq 20$ Oe and $H_s \simeq 45$ Oe. As in our case the MOKE signal gives just a qualitative information, it does not allow to measure the real value of satura-

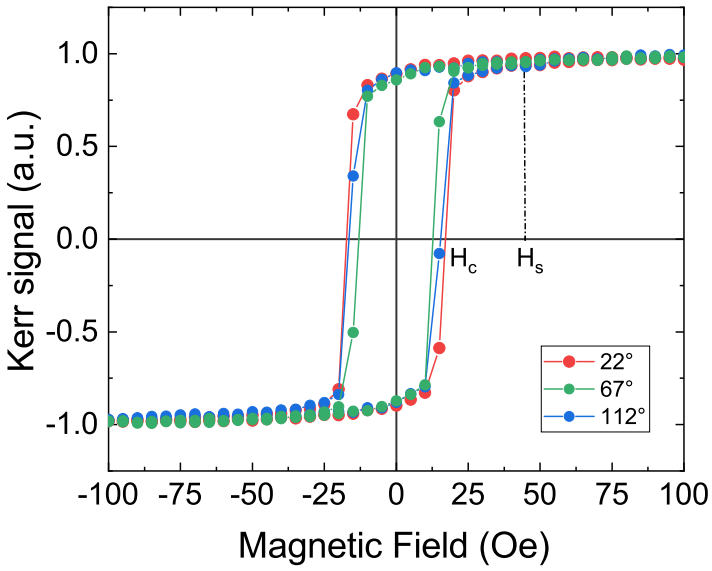

Figura 3.4: Hysteresis loops of the sample at different angles respect to the reference direction (0°) arbitrarily chosen as parallel to one of the sample edges. $H_c \simeq 20$ Oe and $H_s \simeq 45$ Oe are respectively the coercive and the saturation field.

tion magnetization but from literature, we should expect a value of ~ 380 kA m^{-1} [64].

It is worth noting that the entire system consisting in the substrate and the thin film must be considered as the sample, rather than just the thin film. Indeed, the aim of this thesis is to probe the magnetization dynamics driven by the SAWs excited in the substrate by the TG.

3.2 Acoustic characterization of the sample

The sample was acoustically characterized by using the TG spectroscopy.

The laser pulse repetition rate and energy per pulse on sample were chosen in order to be sure not to damage the sample itself. The repetition rate was set at 50 kHz, while the average power, pulse energies and fluences on sample used throughout the experiment are reported in Table 3.2. The measured average power of the two pumps are essentially the same, which is an indication of the high quality of our phase mask.

	Average power (mW)	Pulse energy (nJ)
Left pump	4.8	96
Right pump	4.7	94
Probe	0.045	0.9

Tabella 3.2: Average power and pulse energy on sample of both pumps and probe beams.

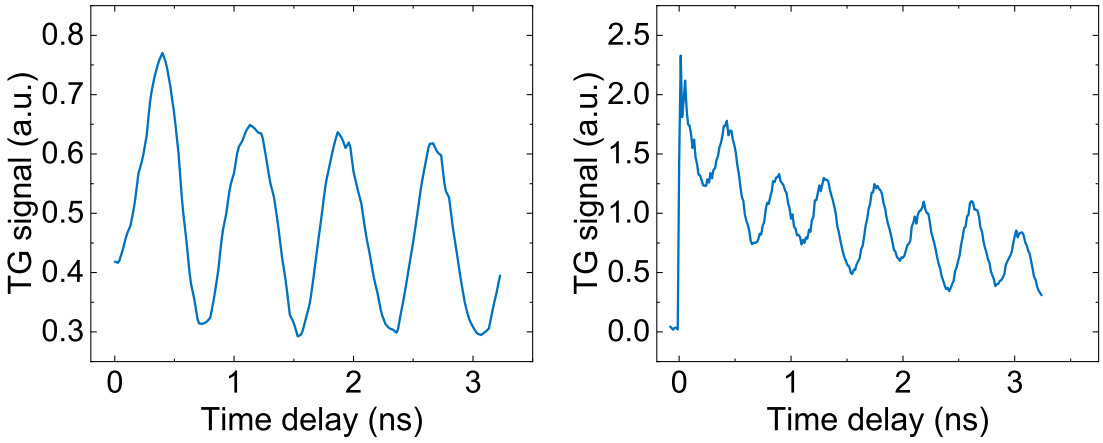

Figura 3.5: Raw TG signals in reflection (left panel) and transmission geometry (right panel). In reflection geometry the coherent peak is not visible because the data acquisition started at a time delay $\tilde{t} > 0$.

We observed the TG signal in both transmission and reflection. The Ni thin film plays a crucial role in the pumps absorption [6], as it was also verified by power measurements. It turned out that $\sim 60\%$ of the incident beam is reflected and just $\sim 6\%$ is transmitted; therefore, $\sim 34\%$ is absorbed. The high absorption in the Ni film, and the subsequent heat transfer in the substrate increase the thermal coupling between pump pulses and material, and so the intensity of the diffracted TG signal.

As mentioned earlier, it is misleading to treat the Ni thin film and the substrate as two separated systems. A more correct approach is to treat the sample as a whole. Indeed, the Ni thin film strongly absorbs the pump energy, building up a superficial temperature grating. Over time, the grating diffuses into the substrate, generating a several µm deep density modulation and involving a consistent portion of the substrate volume. The same effect could be achieved replacing the Ni with any other thin film strongly absorbing at 1030 nm. Of course, in order to study the magnetoelastic coupling a ferromagnetic one is needed.

Figure 3.5 shows the raw TG signals in both reflection and transmission geometry obtained with a TG pitch of $\Lambda = 2.5$ µm ($q = 2.47$ µm^{-1}). Such delay line scans only take few minutes. The same signals after background subtraction and their Fast Fourier Transform (FFT) amplitude are displayed in Figure 3.6. In order to remove the background a linear fit of the raw signal was subtracted. This procedure gives a signal approximately centered around zero and therefore it allows to remove the DC component in the FFT. In order to have a more accurate estimate of the SAWs frequency, the data were zero-filled before calculating the FFT. This whole procedure was followed for each acquired signal presented in this chapter.

The FFT amplitude shows that with this optical technique and geometry we are able to excite and detect two types of waves, which can be identified as the RSAW and the SSLW [6] of the fused quartz substrate. This is clearly visible in the FFT amplitudes, which show two peaks at $f^{RSAW} = 1.32 \pm 0.15$ GHz and $f^{SSLW} = 2.34 \pm 0.15$ GHz, where the error is given by the FWHM of the FFT peak. Therefore, the sound velocity of the RSAW and SSLW are respectively $c_s^{RSAW} = 2\pi f^{RSAW}/q = 3.35$

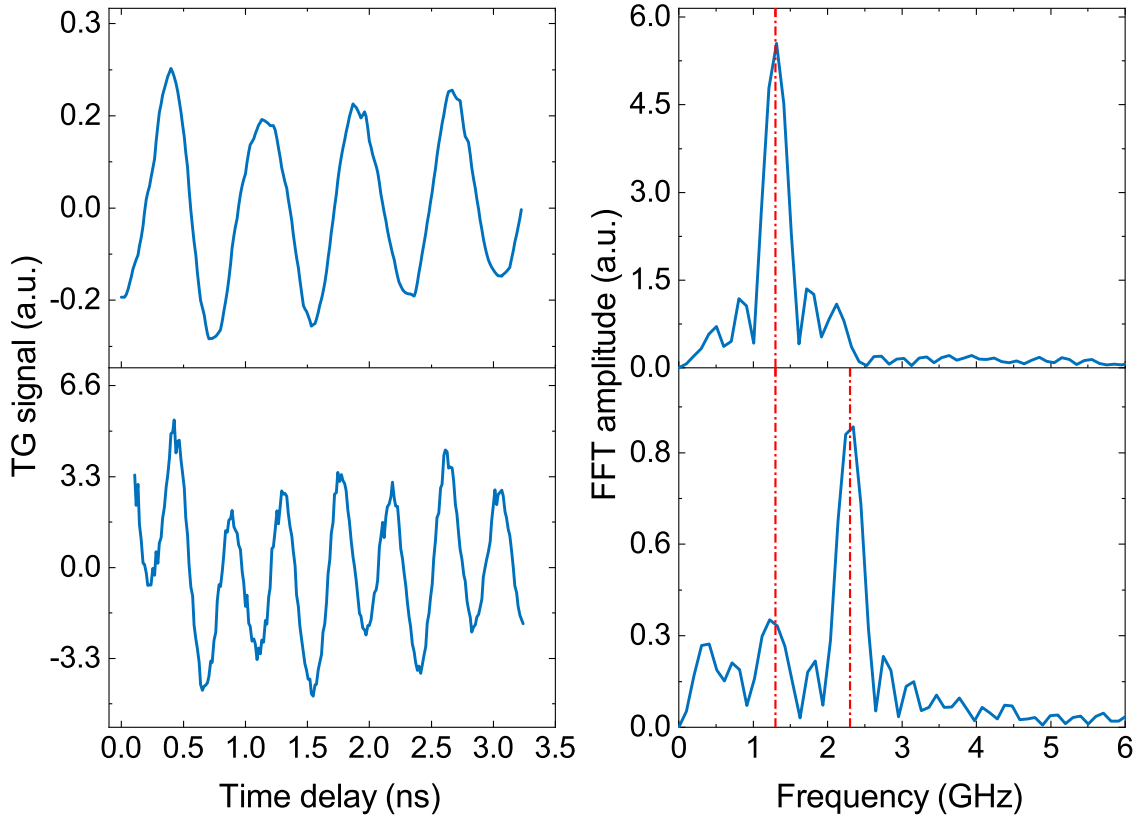

Figura 3.6: TG signals after background subtraction in both reflection and transmission geometry and their relative FFT amplitude. The TG signal in reflection (top left) is more sensitive to the RSAW, while the TG in transmission (bottom left) to the SSLW. The FFT of the TG in reflection (top right) has the main peak at 1.32 GHz, while the one of the TG in transmission (bottom right) is at 2.34 GHz. The red dashed lines in correspondence of these frequencies show that the TG in transmission can probe both waves with different sensitivity.

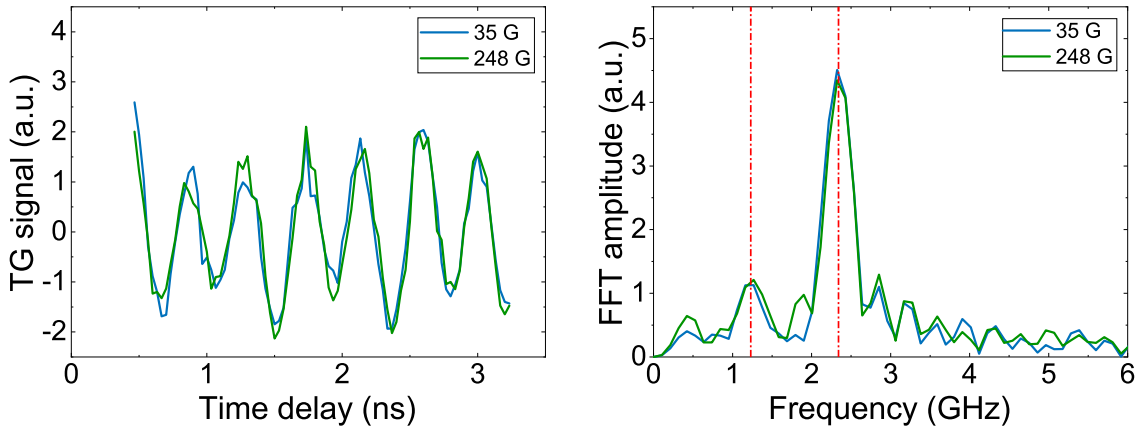

Figura 3.7: TG signals ($\Lambda = 2.5$ µm) in transmission with an external applied magnetic field of 35 and 248 G and their FFT amplitude. The red dashed lines placed at 1.32 and 2.34 GHz show no deviations from the zero field case shown in Figure 3.6

$\mathrm{km\,s^{-1}}$ with a relative error of $\sim 8\%$ and $c_s^{SSLW} = 2\pi f^{SSLW}/q = 5.96\ \mathrm{km\,s^{-1}}$ with a relative error of 6%. The results obtained are in perfect agreement with what reported literature [14]. Additional acoustic modes sustained by the thin film only are not expected, since being $hq \sim 0.01$ the only possible mode is the RSAW of the substrate itself (see Section 1.1).

It is noticeable that the TG signal in reflection configuration is more sensitive to the RSAW, while in transmission to the SSLW. Moreover, in transmission both of them are detectable. This was also observed by Janušonis [6] and theoretically predicted by scattering efficiency calculations [65, 66]. Indeed, the TG in reflection geometry has the surface contribution only, while in transmission has both a bulk and surface contribution. In particular, the latter is identical in reflection and transmission geometry.

Since in our experiment we want to study the magnetoelastic coupling as a function of an external applied magnetic field, we verified that the TG signal is not affected by an applied external magnetic field. Figure 3.7 shows two TG measurements in transmission after background removal and their FFT amplitudes at different applied magnetic fields. As expected, no significant deviations are observed. We can therefore conclude that an external magnetic field does not affect the excitation of the SAWs, and consequently the TG signal.

3.3 Time resolved Faraday probe

This section summarizes the experimental results obtained combining the TG with time-resolved Faraday probe. The raw Faraday signals at three different applied magnetic field values are shown in Figure 3.8. The TG pitch is $\Lambda = 2.5$ µm if not explicitly said otherwise. It is evident that the periodicity of these signals depends on the magnetic field. Similarly to how the TG signals were treated, a linear fit is subtracted to the data to get rid of the DC component of the FFT amplitude. Figure 3.9 shows the signals at different values of applied H field after

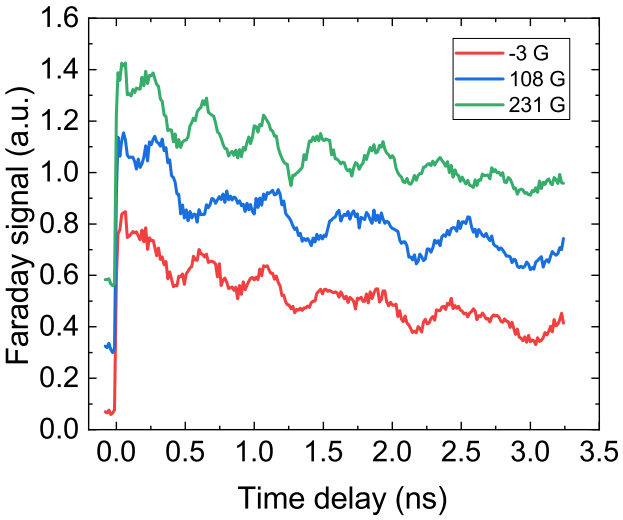

Figura 3.8: Raw time resolved Faraday signals acquired at different applied magnetic fields.

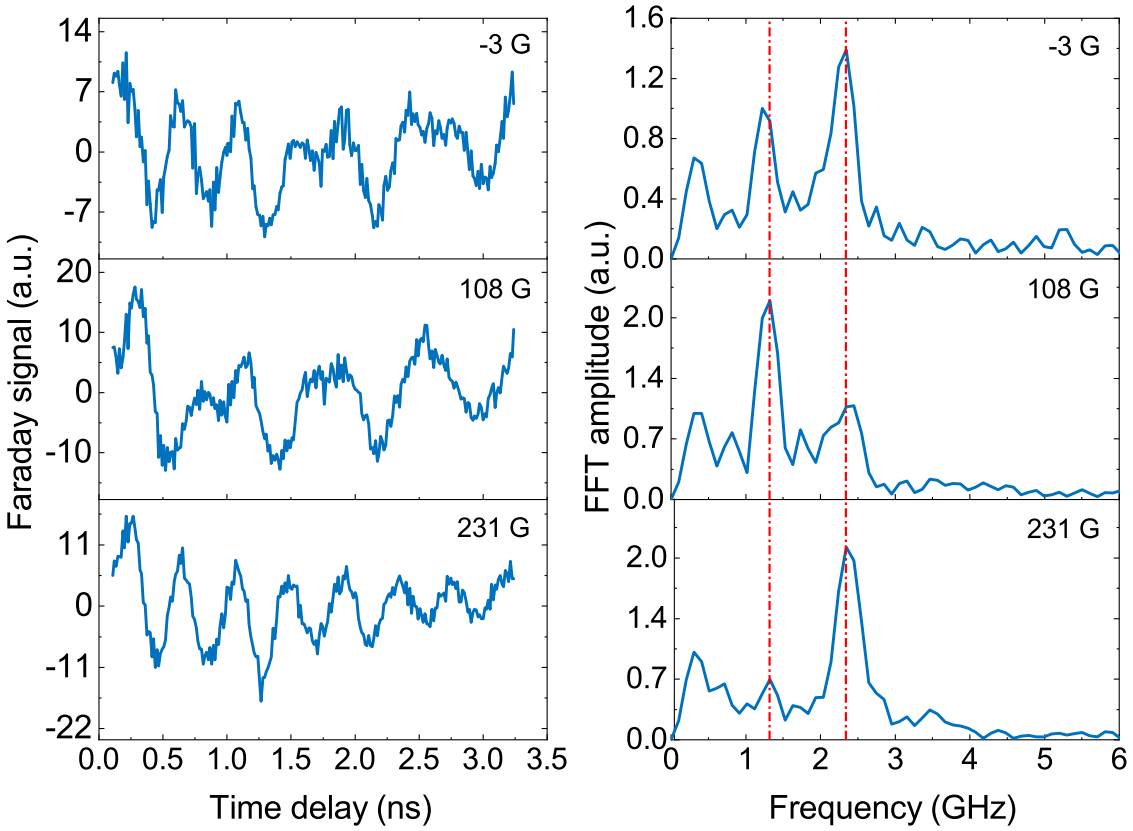

Figura 3.9: Time resolved Faraday signals after background subtraction and their FFT amplitude at three different applied magnetic fields. The red dashed reference lines at 1.32 and 2.34 GHz show that these signals have the same frequencies as the SAWs excited in the sample by the TG. The periodicity of the signals strongly depends on the magnetic field. The peak at ~ 0.3 GHz is an experimental artifact, since it does not depends on the magnetic field.

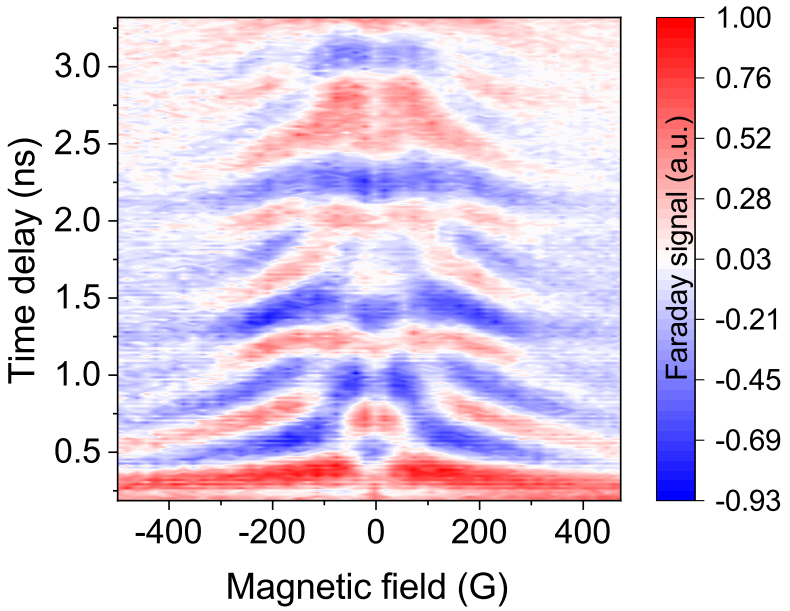

Figura 3.10: Faraday rotation amplitude over time as a function of the applied magnetic field. The signal amplitude and periodicity strongly depends on the magnitude of the applied magnetic field.

background subtraction and their FFT amplitude. As it can be seen, when there is an external field of 108 and 231 G the FFT peaks are at 1.32 and 2.34 GHz, while at -3 G are slightly shifted back at 1.30 and 2.23 GHz; nevertheless, they are compatible within the error of 0.2 GHz estimated from the FWHM of the FFT peaks. They are therefore in perfect agreement with the frequencies found in the acoustic characterization of the sample. These measurements also show how the power spectrum of the Faraday signal strongly depends on the applied magnetic field. In particular, while at very low fields both frequencies are almost equally present, at ~ 100 G and ~ 230 G one spectral component prevails on the other.

In order to systematically investigate this dependence, we performed a magnetic field scan. This scan consists in acquiring the Faraday signal at different magnetic fields, starting from $H = 473$ G and decreasing the magnetic field following the upper branch of the magnetic hysteresis loop shown in Figure 2.16. The sample was brought to saturation before starting the scan. In Figure 3.10 is shown a map of the Faraday signal amplitude over time as a function of the magnetic field. This way of presenting the data allows to better visualize the Faraday rotation changes in both amplitude and periodicity at different magnetic fields.

Let's now analyze these signals in the frequency domain. Figure 3.11 shows the FFT amplitude of each acquired signal as a function of the magnetic field, both as a 2D contour map and a 3D surface. The two dashed reference lines indicate the frequencies of the RSAW and SSLW generated by the TG. This Figure clearly shows that we are looking at elastically driven resonances that exhibit a non-trivial response with the magnetic field. Physically, the resonances are due to elastically driven FMR. When the applied magnetic field makes the magnetic moment precess at the frequency of the TG-generated SAWs, the signal shows an enhancement of

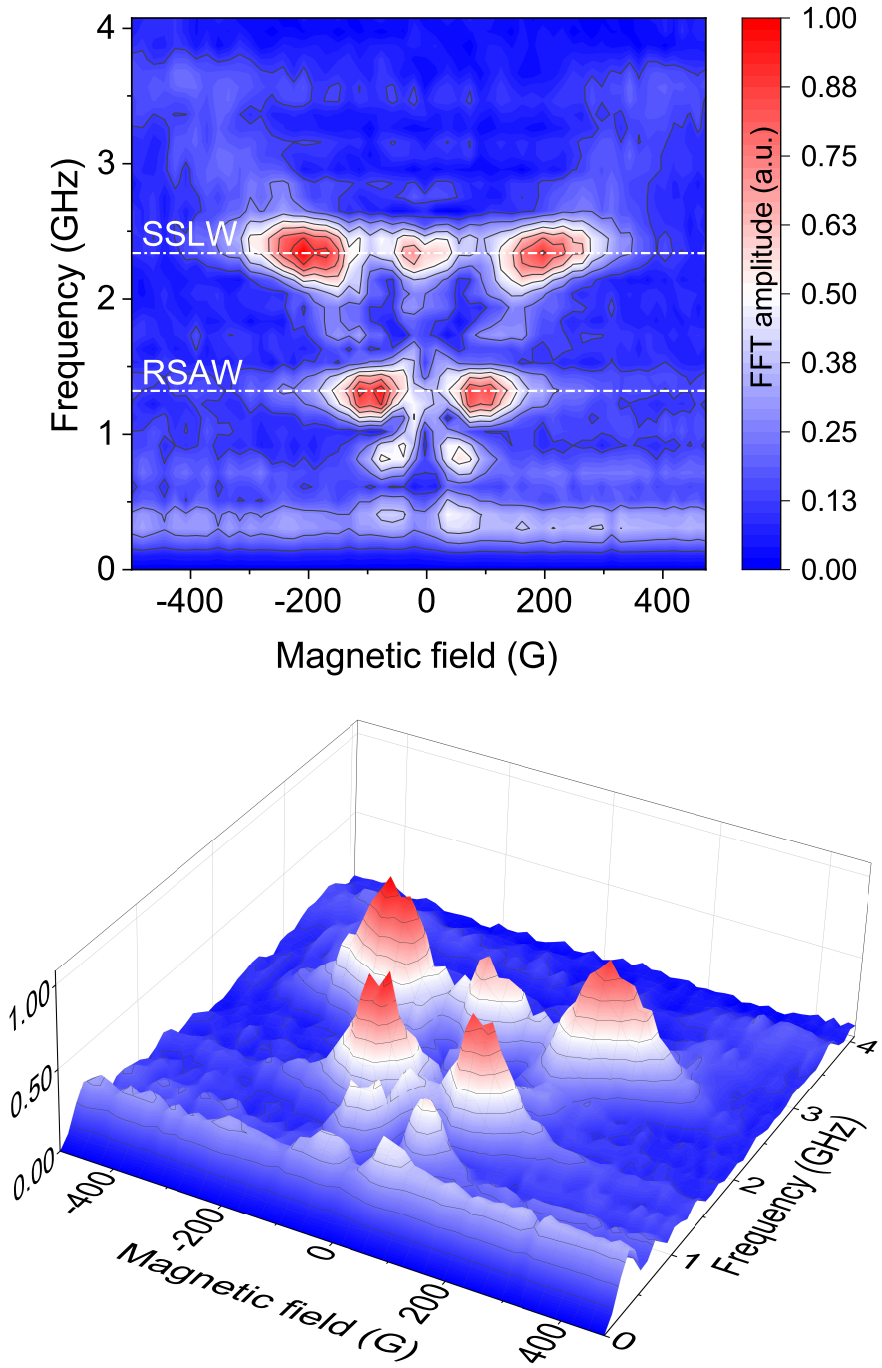

Figura 3.11: FFT amplitude of the Faraday signals as a function of the magnetic field, normalized and represented as a 2D contour map and a 3D surface. The white dashed lines in the 2D map represent the frequencies of the RSAW and the SSLW generated in the sample using the TG. The horizontal field-independent background lines are artifacts due to the zero-filling procedure in the FFT calculation.

the amplitude of the magnetization precession. This means that the elastic and magnetic degrees of freedom couple resonantly and so, at this specific magnetic fields, large precessional dynamics is driven by the SAWs. As expected, both Figure 3.10 and Figure 3.11 shows nearly identical signals when reversing the magnetic field direction (see Section 1.4).

With reference at Figure 2.4, the small field dependent signal at very low fields seems to be related to the angle α between the applied $\vec{H}$ and the $\vec{q}$ of the SAWs [6]. We did this measurements with a small angle of $\alpha \sim 5°$, but it is likely to disappear when this angle is increased. However, this could not be experimentally verified it because at the present time only small α values are possible and this parameter can not be varied systematically. This effect needs to be further investigated. A detailed study on how this angle affects the signal can be found in Reference [49].

Once we validated our setup to be suitable to study the magnetoelastic coupling in a Ni thin film, we repeated the experiment with two more TG pitch, namely $\Lambda = 3$ µm and $\Lambda = 4$ µm. This was easily achieved by changing phase mask. All other experimental parameters were kept fixed. As expected, the frequencies of the RSAW and SSLW change accordingly to the TG pitch, and consequently to the $\vec{q}$. For $\Lambda = 3$ µm we obtained $f^{RSAW} = 1.15 \pm 0.15$ GHz and $f^{SSLW} = 1.91 \pm 0.15$ GHz, while for $\Lambda = 4$ µm we obtained $f^{RSAW} = 0.81 \pm 0.15$ GHz and $f^{SSLW} = 1.50 \pm 0.15$ GHz. The error is estimated as the FWHM of the FFT peaks. These frequencies and the correspondent $\vec{q}$ on sample give velocities consistent with what obtained earlier in the case of $\Lambda = 2.5$ µm and what reported in literature. We performed a magnetic field scan for both Λ. The normalized FFT amplitudes of the signals acquired in the magnetic field scans are shown in Figure 3.12. As expected, clear resonances are observed at the SAWs frequencies, marked with white dashed lines.

As the resonances occur when the SAWs frequency cross the FMR curve of the ferromagnetic thin film, the envelope of the FFT maxima gives the FMR of the Ni thin film. Therefore, combining the results obtained in the magnetic field scans it is possible to derive the saturation magnetization of the Ni thin film. Figure 3.13 shows simultaneously the results obtained for $\Lambda = 2.5$, $\Lambda = 3$ and $\Lambda = 4$ µm and the fit of the FFT maxima for positive magnetic fields using the Kittel formula (see Equation 1.9). The gyromagnetic ratio is kept fixed at 28.02 GHz T^{-1} [64] and the resulting saturation magnetization is $M_s = 238 \pm 20$ kA m^{-1}. Considering that the saturation magnetization of a thin film depends on its growth technique and conditions, this value is consistent with what reported in literature [64].

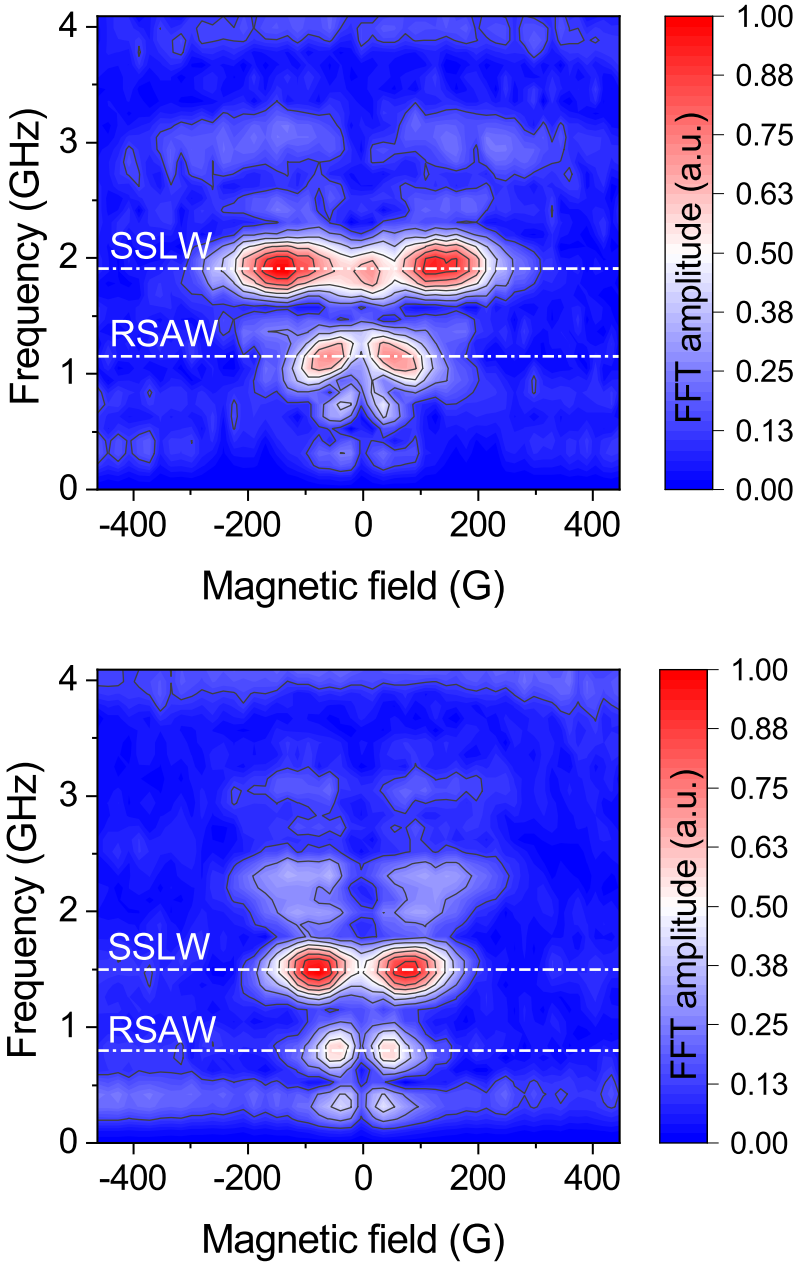

Figura 3.12: FFT amplitude of the Faraday signals as a function of the applied magnetic field, obtained with $\Lambda = 3$ nm (top panel) and $\Lambda = 4$ nm (bottom panel).

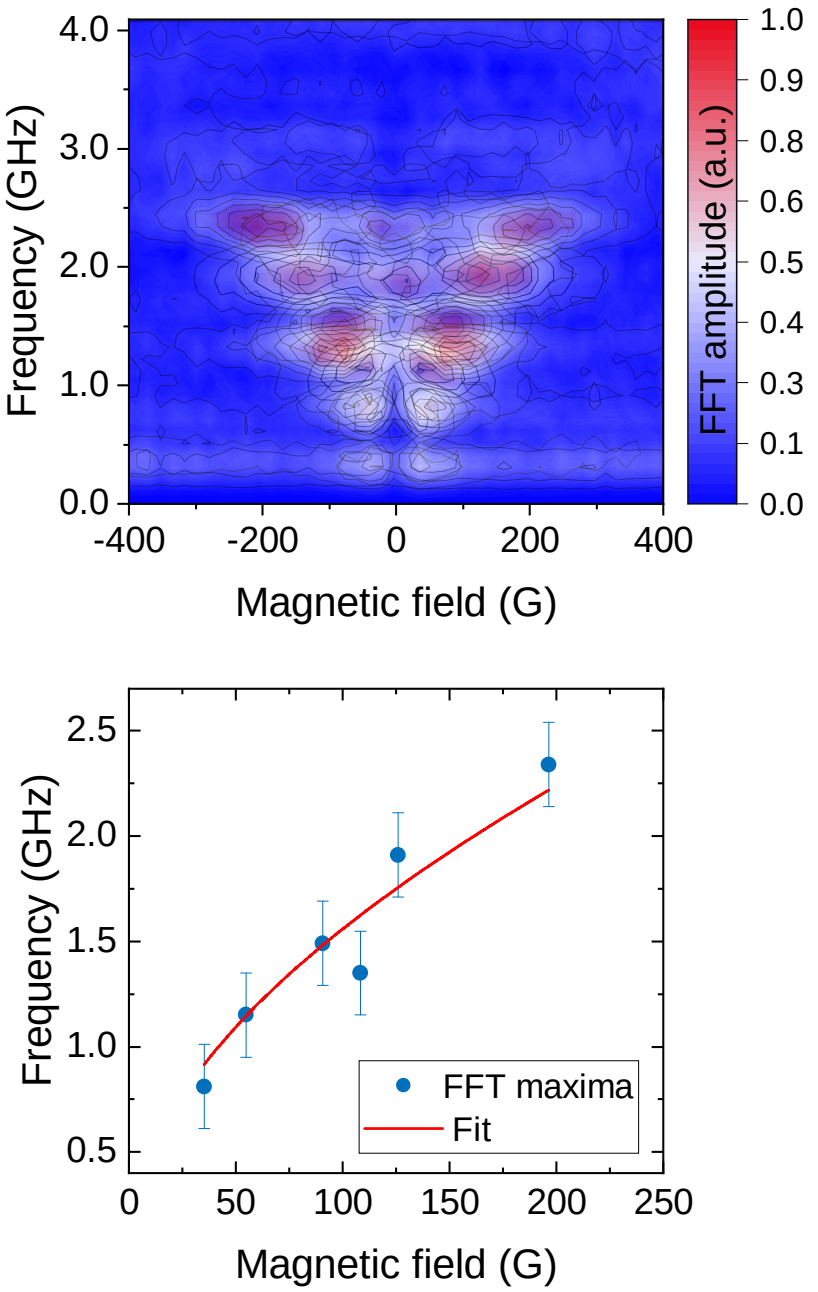

Figura 3.13: Results of the magnetic field scans for $\Lambda = 2.5, 3, 4$ µm (top panel) and FFT maxima fitted using the Kittel formula (bottom panel). The error bars are estimated from the FWHM of the FFT amplitude of the Faraday signals at resonance.

Observation of parametric new frequency generation

The small field-dependent signals in the magnetic field scans at frequencies different from the ones of the TG-generated SAWs (f^{RSAW} and f^{SSLW}) are due to parametric down-conversion, up-conversion and frequency mixing [11]. Down-conversion consists in the generation of a precessional motion with a lower frequency with respect to the one of the SAW, while in up-conversion is higher. Frequency mixing can arise when multiple SAWs are excited, and linear combination of the SAW frequencies are possible. This phenomena can arise from parametric modulation of the magnetization dynamics. Therefore, our system and experimental setup provide an opportunity to investigate such phenomena, where the TG-excited coherent phonons can supply the parametric (elastic) modulation to drive non-trivial magnetization dynamics.

Starting from the linearized Landau-Lifshitz-Gilbert equation in the neighborhood of the equilibrium magnetization direction, the magnetization motion can be expressed as a classical parametric oscillator [11]

$$\frac{\mathrm{d}^2 M}{\mathrm{d}t^2} + \Gamma(t)\frac{\mathrm{d}M}{\mathrm{d}t} + \Big[\Omega_0^2 + \Omega_1^2 \varepsilon_{xx}(t)\Big] M = F_0 \varepsilon_{xx}(t) \tag{3.1}$$

where $F_0\varepsilon_{xx}(t)$ is the external driving force provided by the SAWs and $\Gamma(t) = \Gamma_0 + \Gamma_1\varepsilon_{xx}(t)$ and $\Omega^2(t) = \Omega_0^2 + \Omega_1^2\varepsilon_{xx}(t)$ are respectively the FMR damping and the angular frequency. The parametric dependence is therefore given by the acoustic strain $\varepsilon_{xx}(t)$. It is known [67] that new frequencies can be generated by a classical externally driven parametric oscillator without nonlinear interactions.

Figure 3.14 shows the three magnetic field scans with some additional reference lines to highlight this phenomena. As can be seen, different new frequencies are observed with different grating pitches and the efficiency seems to increase for larger grating pitches. However, the role of the grating pitch in new frequency generation needs further investigations.

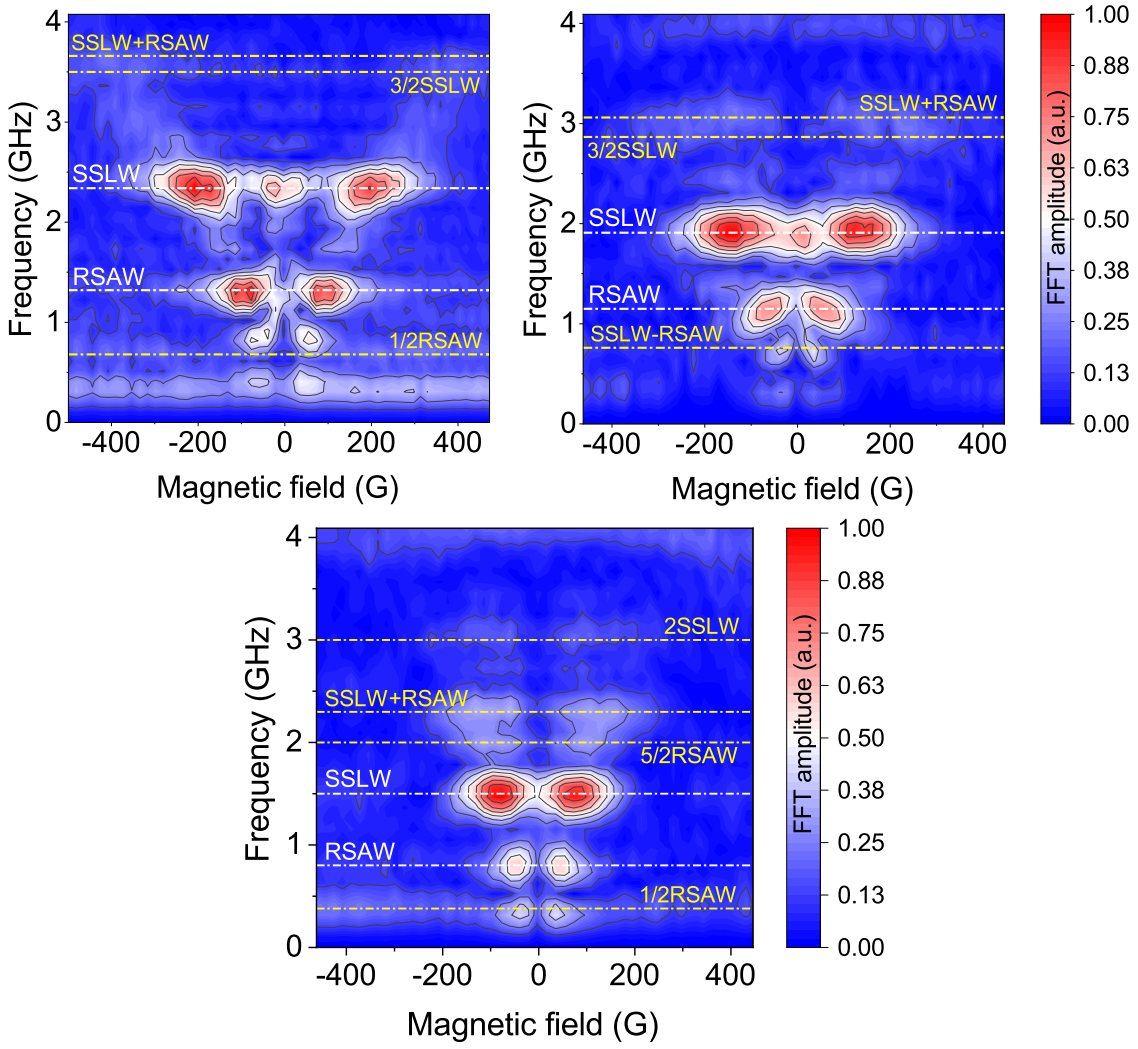

Figura 3.14: FFT amplitude of the Faraday signals as a function of the magnetic field, obtained with $\Lambda = 2.5$ (top left panel), $\Lambda = 3$ (top right panel) and $\Lambda = 4$ µm (bottom panel). The RSAW and the SSLW generated with the TG allow the observation of parametric down-conversion ($f^{RSAW}/2$), up-conversion ($5f^{RSAW}/2$, $3f^{SSLW}/2$, $2f^{SSLW}$) and frequency mixing ($f^{SSLW} + f^{RSAW}$, $f^{SSLW} - f^{RSAW}$).

Conclusion and outlook

The all-optical approach is applied to study magnetoelastic coupling in a ferromagnetic thin film. Taking advantage of the availability of the PHAROS source of laser 300-fs pulses at the NFFA-SPRINT facility of IOM-CNR in the Fermi@Elettra hall at Trieste, we have built an all new experimental setup which is able to combine TG spectroscopy with a time resolved Faraday probe. The operation and performances of the setup were characterized and tested on a 40 nm Ni thin film on a glass substrate.

The acoustical characterization of the sample through TG spectroscopy showed that we are able to excite and detect in the substrate two SAWs, namely the RSAW and the SSLW. As expected from the surface-sensitivity of the TG spectroscopy, in reflection geometry we only detected the RSAW, while both of them are measured in transmission. The frequencies of SAWs launched by the TG are easily calculated from the FFT of the time-resolved TG signal. Due to its small thickness, no contribution of the thin film is detected.

We proved that in our conditions of optics, wavelengths and grating pitches it is possible to observe the elastically driven FMR of the Ni thin film. The elastically driven FMR is detected by the time-resolved Faraday probe. Varying the externally applied magnetic field we observed resonances when the Kittel and acoustic wave frequency match. By changing the TG pitch we could drive the frequency of the TG-generated SAWs, and consequently we could determine the magnetic field values of the corresponding resonances. Therefore, the magnetoelastic coupling provides itself a way to extract the saturation magnetization of the specimen, with a non-invasive and contactless technique. As the Kittel formula describes the envelope of these resonances, we did a fit to estimate the saturation magnetization, which resulted to be 238 ± 20 kA m^{-1}.

Finally, the observation of higher order phenomena, such as down-conversion, up-conversion and frequency mixing suggests that our setup has the sensitivity to perform state-of-the-art measurements.

We did reproduce the state-of-the-art results from the literature. However, some experimental features still need to be understood. An accurate explanation of the background we subtracted in the Faraday signals to remove the DC component of the FFT is still missing, however it could be attributed to the Voigt effect. Furthermore, as for now, we still need to understand the reason why in the magnetic field scans there is a resonance at the frequency of the SSLW only at $H \sim 30$ G, how it is affected by the angle between the external field and the TG-induced acoustic wave wave vector and if it depends on the TG pitch. Indeed, it was observed in two

scans out of three. Further experiments need to be run also to clarify the role of the TG pitch in the observed parametric down-conversion, up-conversion and frequency mixing. It seems that these phenomena are more efficient for bigger TG pitches and it is likely that this is due to a bigger magnetic field range where the two resonances overlap. Finally, we also need to properly investigate if in the magnetic field scans there is a signature of the switching of the magnetization, which could bring additional information about the static magnetic properties of the sample.

Many setup improvements and experiments are scheduled for the immediate future. A research program on the magnetoelastic coupling in complex magnetic systems, such as multiferroics, is planned as a first research application of the method and setup. As for now, we have the magnetic probe only in transmission, we can investigate very thin film or transparent samples only. The implementation of time-resolved MOKE will allows us to work also in reflection, making the setup more versatile and suitable to study a rich variety of quantum materials. Moreover, by changing the polarization of the two pumps, some interesting physics could arise in more complex magnetic systems, such as spin grating and skyrmions. Finally, a vacuum chamber with a cryostat will be soon installed. It will allow to work in more controlled sample experimental conditions and to perform temperature-dependent measurements to study phase transitions and complex spin dynamics. It will furthermore allow to transfer, under UHV, samples as grown by laser ablation or molecular beam epitaxy, without need of protective layers and suitable for the study of pristine surface properties. The whole setup has been developed in the framework of the NFFA-SPRINT facility development, in close collaboration with PhD student Pietro Carrara and Dr. Riccardo Cucini, and in the broader environment of the NFFA-SPRINT and NFFA-APE collaborations.

List of abbreviations

AFM	Atomic Force Microscopy
APE	Advanced Photoelectric Effect experiments
APE-HE	Advanced Photoelectric Effect experiments-High Energy
BBO	Beta-Barium Borate
CNR	Consiglio Nazionale delle Ricerche
EM	Electromagnetic
FFT	Fast Fourier Transform
FWHM	Full Width at Half Maximum
IDT	InterDigitated Transducer
IOM	Institute Of Materials
MOKE	Magneto Optical Kerr Effect
NFFA	Nano Foundries and Fine Analysis
RSAW	Rayleigh Surface Acoustic Wave
SAW	Surface Acoustic Wave
SHG	Second Harmonic Generation
SPRINT	Spin Polarization Research Instrument in the Nanoscale and Time domain
SSLW	Surface Skimming Longitudinal Wave
TG	Transient Grating
THG	Third Harmonic Generation

Bibliography

[1] M Mitchell Waldrop. «More than moore». In: *Nature* 530.7589 (2016), pp. 144–148.

[2] S D Sarma et al. «Issues, concepts, and challenges in spintronics». In: *58th DRC. Device Research Conference. Conference Digest (Cat. No. 00TH8526)*. IEEE. 2000, pp. 95–98.

[3] W G Yang e H Schmidt. «Acoustic control of magnetism toward energy-efficient applications». In: *Applied Physics Reviews* 8.2 (2021), p. 021304.

[4] M Weiler et al. «Elastically driven ferromagnetic resonance in nickel thin films». In: *Physical review letters* 106.11 (2011), p. 117601.

[5] L Dreher et al. «Surface acoustic wave driven ferromagnetic resonance in nickel thin films: Theory and experiment». In: *Physical Review B* 86.13 (2012), p. 134415.

[6] J Janušonis et al. «Transient grating spectroscopy in magnetic thin films: Simultaneous detection of elastic and magnetic dynamics». In: *Scientific reports* 6.1 (2016), pp. 1–10.

[7] A V Mamishev et al. «Interdigital sensors and transducers». In: *Proceedings of the IEEE* 92.5 (2004), pp. 808–845.

[8] R Torre. *Time-resolved spectroscopy in complex liquids*. Springer, 2007.

[9] H C Siegmann J Stöhr. *Magnetism: From Fundamentals to Nanoscale Dynamics*. 1ª ed. 152. Springer-Verlag Berlin Heidelberg, 2006.

[10] C Kittel e P McEuen. *Introduction to solid state physics*. Vol. 8. Wiley New York, 1996.

[11] CL Chang et al. «Parametric frequency mixing in a magnetoelastically driven linear ferromagnetic-resonance oscillator». In: *Physical Review B* 95.6 (2017), p. 060409.

[12] W Hassan e P B Nagy. «Simplified expressions for the displacements and stresses produced by the Rayleigh wave». In: *The Journal of the Acoustical Society of America* 104.5 (1998), pp. 3107–3110.

[13] H Lüth. *Surfaces and interfaces of solid materials*. Springer Science & Business Media, 2013.

[14] P Kuszewski. «Optical detection of magneto-acoustic dynamics». Tesi di dott. Sorbonne Université, 2018.

[15] I Kolarov. «Non-destructive testing of surface defects by Rayleigh wave». In: *Machines. Technologies. Materials.* 8.3 (2014), pp. 48–50.

[16] L Bo et al. «Surface acoustic wave devices for sensor applications». In: *Journal of Semiconductors* 37.2 (2016), p. 021001.

[17] V Polewczyk et al. «Reversible response of a magnetic surface acoustic wave device with perpendicular magnetization». In: *Journal of Physics D: Applied Physics* 53.30 (2020), p. 305002.

[18] C Bescond et al. «Determination of residual stresses using laser-generated surface skimming longitudinal waves». In: *Nondestructive Evaluation and Health Monitoring of Aerospace Materials, Composites, and Civil Infrastructure IV*. Vol. 5767. International Society for Optics e Photonics. 2005, pp. 175–186.

[19] PD Bloch et al. «Observations on surface skimming bulk waves and other waves launched from an IDT on lithium niobate». In: *1981 Ultrasonics Symposium*. IEEE. 1981, pp. 268–273.

[20] S Sathish, R W Martin e T J Moran. «Local surface skimming longitudinal wave velocity and residual stress mapping». In: *The Journal of the Acoustical Society of America* 115.1 (2004), pp. 165–171.

[21] C Caliendo e M Hamidullah. «Guided acoustic wave sensors for liquid environments». In: *Journal of Physics D: Applied Physics* 52.15 (2019), p. 153001.

[22] Y Huang, P K Das e V R Bhethanabotla. «Surface acoustic waves in biosensing applications». In: *Sensors and Actuators Reports* (2021), p. 100041.

[23] M Lewis. «Surface skimming bulk wave, SSBW». In: *1977 Ultrasonics Symposium*. IEEE. 1977, pp. 744–752.

[24] J A Rogers et al. «Optical generation and characterization of acoustic waves in thin films: Fundamentals and applications». In: *Annual Review of Materials Science* 30.1 (2000), pp. 117–157.

[25] H J Eichler, P Günter e D W Pohl. *Laser-induced dynamic gratings*. Vol. 50. Springer, 2013.

[26] S Adachi et al. «Optical sampling four-wave-mixing experiment for exciton relaxation processes». In: *Optics communications* 174.1-4 (2000), pp. 291–298.

[27] T S Rose e MD Fayer. «Probing gas-phase dynamics with picosecond transient grating spectroscopy». In: *Chemical physics letters* 117.1 (1985), pp. 12–17.

[28] E J Brown, Q Zhang e M Dantus. «Femtosecond transient-grating techniques: Population and coherence dynamics involving ground and excited states». In: *The Journal of chemical physics* 110.12 (1999), pp. 5772–5788.

[29] J Janušonis et al. «Frequency tunable surface magneto elastic waves». In: *Applied Physics Letters* 106.18 (2015), p. 181601.

[30] J Janušonis et al. «Ultrafast magnetoelastic probing of surface acoustic transients». In: *Physical Review B* 94.2 (2016), p. 024415.

[31] Y Yan e K A Nelson. «Impulsive stimulated light scattering. I. General theory». In: *The Journal of chemical physics* 87.11 (1987), pp. 6240–6256.

[32] L Dhar, J A Rogers e K A Nelson. «Time-resolved vibrational spectroscopy in the impulsive limit». In: *Chemical Reviews* 94.1 (1994), pp. 157–193.

[33] A Taschin. «Relaxation processes on supercooled liquids by heterodyne detected transient grating experiment.» Tesi di dott. Università degli studi di Firenze.

[34] AR Cameron, P Riblet e A Miller. «Spin gratings and the measurement of electron drift mobility in multiple quantum well semiconductors». In: *Physical review letters* 76.25 (1996), p. 4793.

[35] R Cucini. «Transport processes in nano-heterogeneous materials by Transient Grating experiments». Tesi di dott. Università degli studi di Firenze, 2008.

[36] S Suresh et al. «Review on theoretical aspect of nonlinear optics». In: *Rev. Adv. Mater. Sci* 30.2 (2012), pp. 175–183.

[37] M Fox. *Optical Properties of Solids*. Oxford master series in condensed matter physics. Oxford University Press, 2001.

[38] J W Goodman. *Introduction to Fourier optics*. Roberts e Company Publishers, 2005.

[39] G New. *Frequency mixing*. Cambridge University Press, 2011, pp. 19–44. DOI: 10.1017/CBO9780511975851.003.

[40] N Bloembergen. «Conservation laws in nonlinear optics». In: *JOSA* 70.12 (1980), pp. 1429–1436.

[41] CW Thiel. «Four-wave mixing and its applications». In: *Faculty of Washington, Washington DC* (2008).

[42] H Montiel e G Alvarez. «Detection of magnetic transitions by means of ferromagnetic resonance and microwave absorption techniques». In: *Ferromagnetic Resonance-Theory and Applications*. Intech Rijeka, Croatia, 2013.

[43] Z Celinski, KB Urquhart e B Heinrich. «Using ferromagnetic resonance to measure the magnetic moments of ultrathin films». In: *Journal of Magnetism and Magnetic Materials* 166.1-2 (1997), pp. 6–26.

[44] M Oogane et al. «Magnetic damping in ferromagnetic thin films». In: *Japanese journal of applied physics* 45.5R (2006), p. 3889.

[45] Y Pu et al. «Spin accumulation detection of FMR driven spin pumping in silicon-based metal-oxide-semiconductor heterostructures». In: *arXiv preprint arXiv:1311.0965* (2013).

[46] VE Demidov et al. «Wide-range control of ferromagnetic resonance by spin Hall effect». In: *Applied Physics Letters* 99.17 (2011), p. 172501.

[47] Y Wang, R Ramaswamy e H Yang. «FMR-related phenomena in spintronic devices». In: *Journal of Physics D: Applied Physics* 51.27 (2018), p. 273002.

[48] NB Ekreem et al. «An overview of magnetostriction, its use and methods to measure these properties». In: *Journal of Materials Processing Technology* 191.1-3 (2007), pp. 96–101.

[49] CL Chang. «Opto-magnonic Crystals: Optical Manipulation of Spin Waves». Tesi di dott. University of Groningen, 2019.

[50] M Weiler. «Mgnon-phonon interactions in ferromagnetic thin films». Tesi di dott. Technischen Universität München, 2012.

[51] D Labanowski et al. «Voltage-driven, local, and efficient excitation of nitrogen-vacancy centers in diamond». In: *Science advances* 4.9 (2018), eaat6574.

[52] T Jansma. «Transient Grating Spectroscopy of Magnetic Thin Films». University of Groningen, 2016.

[53] R Schafer A Hubert. *Magnetic Domains: The Analysis of Magnetic Microstructures*. Corrected. Springer, 2008.

[54] T Haider. «A review of magneto-optic effects and its application». In: *Int. J. Electromagn. Appl* 7.1 (2017), pp. 17–24.

[55] Ml Freiser. «A survey of magnetooptic effects». In: *IEEE Transactions on magnetics* 4.2 (1968), pp. 152–161.

[56] Zurich instrument. *White paper*. URL: `https://www.zhinst.com/europe/en/lock-in-amplifiers`.

[57] KG Libbrecht, ED Black e CM Hirata. «A basic lock-in amplifier experiment for the undergraduate laboratory». In: *American Journal of Physics* 71.11 (2003), pp. 1208–1213.

[58] A A Maznev, T F Crimmins e K A Nelson. «How to make femtosecond pulses overlap». In: *Opt. Lett.* 23.17 (set. 1998), pp. 1378–1380. DOI: `10.1364/OL.23.001378`.

[59] A Yu Meshalkin et al. «Analysis of diffraction efficiency of phase gratings in dependence of duty cycle and depth». In: 1368.2 (2019), p. 022047.

[60] NFFA. *Ultraviolet lithography*. URL: `https://www.nffa.eu/offer/lithography-patterning/installation-1/uvl/`.

[61] NFFA. *Physical vapor deposition*. URL: `https://www.trieste.nffa.eu/techniques/growth/pvd/`.

[62] P Mantegazza. «E-field effect on the Fe/PMN-PT heterostructure morphology and magnetism». Università degli Studi di Milano, 2019.

[63] G Vinai et al. «An integrated ultra-high vacuum apparatus for growth and in situ characterization of complex materials». In: *Review of Scientific Instruments* 91.8 (2020), p. 085109.

[64] M C Giordano et al. «Plasma-enhanced atomic layer deposition of nickel nanotubes with low resistivity and coherent magnetization dynamics for 3D spintronics». In: *ACS Applied Materials & Interfaces* 12.36 (2020), pp. 40443–40452.

[65] IM Fishman et al. «Surface selectivity in four-wave mixing: transient gratings as a theoretical and experimental example». In: *JOSA B* 8.9 (1991), pp. 1880–1888.

[66] IM Fishman et al. «Transient grating diffraction from an interface between two materials: theory and experimental application». In: *JOSA B* 10.6 (1993), pp. 1006–1016.

[67] E I Butikov. «Parametric excitation of a linear oscillator». In: *European Journal of Physics* 25.4 (2004), p. 535.